Weather and Climate Dynamics

Future changes in North Atlantic winter cyclones in CESM-LE – Part 1: Cyclone intensity, potential vorticity anomalies, and horizontal wind speed

Edgar Dolores-Tesillos[1]**, Franziska Teubler**[2]**, and Stephan Pfahl**[1]

[1]Institute of Meteorology, Freie Universität Berlin, Berlin, Germany
[2]Institute for Atmospheric Physics, Johannes Gutenberg-Universität Mainz, Mainz, Germany

Correspondence: Edgar Dolores-Tesillos (edgar.dolores@met.fu-berlin.de)

Abstract. Strong low-level winds associated with extratropical cyclones can have substantial impacts on society. The wind intensity and the spatial distribution of wind maxima may change in a warming climate; however, the involved changes in cyclone structure and dynamics are not entirely clear. Here, such structural changes of strong North Atlantic cyclones in a warmer climate close to the end of the current century are investigated with storm-relative composites based on Community Earth System Model Large Ensemble (CESM-LE) simulations. Furthermore, a piecewise potential vorticity inversion is applied to associate such changes in low-level winds to changes in potential vorticity (PV) anomalies at different levels. Projected changes in cyclone intensity are generally rather small. However, using cyclone-relative composites, we identify an extended wind footprint southeast of the center of strong cyclones, where the wind speed tends to intensify in a warmer climate. Both an amplified low-level PV anomaly driven by enhanced diabatic heating and a dipole change in upper-level PV anomalies contribute to this wind intensification. On the contrary, wind changes associated with lower- and upper-level PV anomalies mostly compensate for each other upstream of the cyclone center. Wind changes at upper levels are dominated by changes in upper-level PV anomalies and the background flow. Altogether, our results indicate that a complex interaction of enhanced diabatic heating and altered non-linear upper-tropospheric wave dynamics shape future changes in near-surface winds in North Atlantic cyclones.

1 Introduction

Extratropical or midlatitude cyclones strongly modulate weather and climate in the North Atlantic region. For example, as the cyclones control cloud amount, they regulate the radiation received by the extratropics. Storm tracks are the areas where extratropical cyclones are most likely to form, propagate, dissipate, and contribute the most energy and momentum transport (Chang et al., 2002; Shaw et al., 2016). Extratropical cyclones passing across the midlatitudes generate specific weather conditions (Catto, 2016). Cyclones and associated fronts produce locally up to 90 % of annually accumulated precipitation (Catto et al., 2012; Hawcroft et al., 2012) and also contribute significantly to extreme precipitation events (Catto and Pfahl, 2013; Pfahl et al., 2014). In addition, cyclones can lead to the formation of strong winds (Browning, 2004; Leckebusch et al., 2006). The economic losses due to these winds have been shown to scale approximately with the third power of the near-surface wind speed (Klawa and Ulbrich, 2003; Roberts et al., 2014). The strongest near-surface winds typically occur in the dry intrusion region behind the cold front and the cold conveyor belt, sometimes associated with sting jets (Clark and Gray, 2018), as well as in the warm region to the southeast of the storm center, ahead of the cold front (Hewson and Neu, 2015; Shaw et al., 2016; Slater et al., 2017).

Several conceptual models have been developed to describe cyclone types and structures, such as the Norwegian cyclone model (Bjerknes, 1919) and the Shapiro and Keyser (1990) conceptual model. Airstreams linked to cyclones are described in a three-dimensional conceptual model that in-

corporates warm and cold conveyor belts (Browning, 1990; Wernli and Davies, 1997; Madonna et al., 2014). A helpful variable to analyze midlatitude atmospheric dynamics and the development of cyclones is potential vorticity (PV) (e.g., Hoskins et al., 1985). PV is a conserved quantity under adiabatic conditions; its rate of change is then determined by advection. Any further changes can be attributed to the generation or destruction of PV by non-conservative processes, like diabatic processes (latent heating (LH) and radiative heating) and frictional forcing (Bluestein, 1992; Catto, 2016). A qualitative framework to understand the relation between PV and extratropical cyclone dynamics and the role of LH is through three anomalous components in the PV-associated cyclone circulation: a positive upper-tropospheric PV anomaly, a positive potential temperature anomaly at the surface, and a positive lower-tropospheric PV anomaly (Davis and Emanuel, 1991; Davis, 1992). The positive lower-tropospheric PV anomaly is primarily generated by diabatic processes, in particular, latent heat release during cloud formation (Stoelinga, 1996; Ahmadi-Givi et al., 2004; Büeler and Pfahl, 2017), and can thus be regarded as a proxy for the influence of such diabatic processes on cyclone dynamics. The relative contributions of these anomalies to the wind field and the cyclone intensity can be determined by applying PV inversion techniques (Davis and Emanuel, 1991; Davis, 1992; McTaggart-Cowan et al., 2003; Tochimoto and Niino, 2016; Flaounas et al., 2021).

Anthropogenic climate change is expected to lead to alterations also in the spatial distribution and properties of extratropical cyclones. Projections from climate models have been analyzed to identify such cyclone changes in a warming climate (Ulbrich et al., 2009; Zappa et al., 2013; Raible et al., 2018; Sinclair et al., 2020). While future changes in the North Pacific and, in particular, the Southern Ocean are, to first order, characterized by a poleward shift of storm tracks (O'Gorman, 2010), the pattern of projected changes in the North Atlantic region is more complex (Ulbrich et al., 2009; Zappa et al., 2013). Such changes in the spatial distribution and intensity of cyclones are thought to result from a tug-of-war (Shaw et al., 2016) between different processes, such as changes in horizontal temperature gradients and baroclinicity, vertical stability, tropopause height, and latent heat release (O'Gorman and Schneider, 2008; Pfahl et al., 2015). In particular, the increase in atmospheric moisture content in a warming climate results in an increase also of latent heat release and, therefore, might intensify cyclones. Such a potential intensification may, however, be compensated for by other factors such as an increase in static stability (which is also linked to the moisture increase, in particular in lower latitudes where the atmospheric stratification is closer to a moist adiabatic) (Catto et al., 2019). One way to identify the influence of altered LH on cyclone dynamics is via the PV framework. As the PV anomaly in the lower troposphere is primarily related to diabatic processes, increased LH is expected to result in an intensification of this anomaly. Accord-

ingly, an increase in lower-tropospheric PV in midlatitude cyclones has been detected in idealized model simulations (Pfahl et al., 2015; Büeler and Pfahl, 2019; Sinclair et al., 2020) and climate change studies with regional models (Marciano et al., 2015; Michaelis et al., 2017; Zhang and Colle, 2018). Tamarin and Kaspi (2017) and Tamarin-Brodsky and Kaspi (2017), using PV inversion, showed that such diabatically induced low-level PV increases contribute to an enhanced poleward motion of cyclones as the climate warms. Nevertheless, it is not clear how (diabatic) PV changes link to structural changes in other impact-relevant cyclone properties such as low-level wind velocity. This is one of the central questions of the present study.

Generally, there is a decrease in extratropical cyclone winds projected in the Northern Hemisphere as the climate warms, which reduces the wind hazards associated with the cyclones (Catto et al., 2019). Nevertheless, there may still be specific regions that will experience an increase in wind hazards, such as central and western Europe (Donat et al., 2010; Mölter et al., 2016). In addition, uncertainty in such estimated wind changes arises from the fact that global climate models cannot explicitly represent high-wind-producing mesoscale circulation structures such as sting jets (Martínez-Alvarado et al., 2018). Information on structural changes in extratropical cyclone winds and other properties can be obtained with the help of composite analyses (e.g., Bengtsson et al., 2009; Catto et al., 2010; Dacre et al., 2012; Yettella and Kay, 2017; Pinto and Ludwig, 2020). While idealized modeling experiments point to a broadening of the cyclones' strong wind footprint (Sinclair et al., 2020), composite changes from other regional model studies are relatively noisy (Michaelis et al., 2017), which might be partially related to limited statistics. Here this will be addressed with the help of extensive ensemble simulations providing multiple samples also of extreme North Atlantic cyclones and their future changes.

This study adopts a composite perspective to study future changes in PV anomalies and associated wind changes in North Atlantic cyclones. The paper is organized as follows. In Sect. 2, we introduce the CESM-LE dataset. Section 3 presents the cyclone tracking scheme, composite technique, and PV inversion (PPVI) method. In Sect. 4, results are presented of simulated future changes in cyclone tracks, and the changes in properties of intense cyclones are studied in more detail using composite analysis and PPVI. Conclusions are provided in Sect. 5.

2   Data

We use 6-hourly output from 10 members of the CESM-LE-ETH model ensemble, which were restarted from Community Earth System Model Large Ensemble (CESM-LE) simulations (Kay et al., 2015). The members differ by a small random perturbation to their initial air temperature field on

the order of 10^{-14} K. Each member has a horizontal resolution of $0.94° \times 1.25°$, latitude and longitude, respectively. The vertical coordinate is a hybrid sigma-pressure system with 30 levels. Two periods are analyzed: 1990–2000 for the present-day climate and 2091–2100 for future climate. Historical forcing (Lamarque et al., 2010) was applied in the present-day period and Representative Concentration Pathway 8.5 (RCP8.5) forcing (Meinshausen et al., 2011; Lamarque et al., 2011) in the future period. The simulations have been rerun for these periods (using restart files from the original simulations) to obtain more comprehensive 6-hourly output fields, such as vertical velocity on model levels. Note that the reruns are not bit-identical to the original CESM-LE simulations.

To assess the ability of CESM-LE to simulate observed cyclone track density and statistics, the historical simulations (1990–2000) are compared with the ERA-Interim reanalysis (Dee et al., 2011) for the period 1979–2010.

3 Methods

3.1 Cyclone identification

Cyclones are identified with an updated version of the sealevel pressure (SLP) contour method developed by Wernli and Schwierz (2006), as described in Sprenger et al. (2017). Cyclone centers are defined as local minima in the SLP field. Starting from every SLP minimum, closed isobars are identified at intervals of 0.5 hPa, and the outermost contour that does not exceed 7500 km in length is used as the outer boundary of the system. Cyclones that are close to each other (e.g., binary cyclones with two local SLP minima) are merged as long as the outermost closed contour's length does not exceed 7500 km, and only the deepest SLP minimum of each cyclone is kept and used for cyclone tracking. Successive SLP minima are connected to form a cyclone track if they occur within a specific search area determined by the previous cyclone trajectory. As in Pfahl et al. (2015), only cyclone tracks are taken into account in the following with a minimum lifetime of 24 h and an SLP difference of at least 1 hPa between the minimum and the outermost contour at each time step. Following Neu et al. (2013) the track density is defined as the number of tracks passing a grid cell (with repeated entries of the same track being counted as one). Then, a regridding procedure is applied to project the trajectories onto a regular $1° \times 1°$ grid.

In this study, we focus on analyzing future cyclone changes over the North Atlantic region (30 to 90° latitude, −100 to 40° longitude) for the extended winter season (October–March). We associate a cyclone track to the domain if it has at least one location inside the domain. Therefore, our analysis is based on more than 35 800 storms in the 11 extended winters of present-day climate and more than

30 800 storms in the 10 winters of future climate, pooling the data from all 10 ensemble members.

3.2 Composite analysis

Cyclone-centered composites are created for the strongest 10 % of storms occurring over the North Atlantic region (denoted as intense cyclones in the following), selected by their maximum relative vorticity at 850 hPa averaged over a radius of 250 km around the cyclone center (SLP minimum). Various fields are composited for the time of maximum intensity in accordance with the 850 hPa relative vorticity ($t = 0$), as well as previous hours ($t = -24, -18, -12, -6$ h) and later hours ($t = +6, +12, +18, +24$ h). A radial grid with the pole centered on the cyclone center is generated, covering a spherical cap with a fixed radius of 10°. Meteorological fields are then extracted to this new radial coordinate system and averaged over the chosen extratropical cyclones. The coordinate transformation reduces the distortion due to change in zonal grid spacing with latitude, as described in previous studies (Bengtsson et al., 2009; Catto et al., 2010). In some previous studies, this spherical cap has been rotated in the direction of cyclone propagation. We have tested such a rotation and decided not to use it because it introduced some noise in the composites (e.g., frontal structures appeared to be less apparent in the rotated compared to the unrotated composites; see Fig. S1 in the Supplement).

A complementary perspective on cyclone dynamics is obtained by constructing PV anomalies and PV anomaly profiles. To this end, a PV climatology is defined as follows: firstly, the daily mean PV for each calendar day is calculated at each grid point and each vertical level of the model, separately for present-day (1990–2000) and future (2091–2100) climate. Then, a 30 d window is selected relative to each cyclone position, and composites (as described previously) are obtained, averaged over the 30 d, on different interpolated pressure levels (1000, 925, 850, 750, 700, 600, 500, 400, 300, 250, 200, 150 hPa) from the daily PV dataset. PV anomalies are then defined relative to this 30 d average. Finally, PV anomalies are spatially averaged in a radius of 2.5° around to the cyclone center to construct the PV anomaly profiles.

3.3 Piecewise PV inversion

Piecewise potential vorticity inversion (PPVI) can be used to examine the contributions of PV anomalies (q') to the wind field of an extratropical cyclone (Davis and Emanuel, 1991; Tochimoto and Niino, 2016). For a suitable set of balance and boundary conditions, the invertibility of PV allows the derivation of wind and geopotential height fields from the PV distribution (Hoskins et al., 1985; Seiler, 2019)

With PPVI, q' in extratropical cyclones is commonly partitioned into three layers: the surface layer, the lower atmospheric layer, and the upper atmospheric layer (Seiler, 2019). The inversion may then be utilized to investigate the relative

contributions of the PV anomalies in these layers to the flow field at specific levels (Tamarin and Kaspi, 2016; Teubler and Riemer, 2016; Tamarin-Brodsky and Kaspi, 2017) or to extratropical cyclone intensity (Seiler, 2019). Ertel (1942) defines PV as

$$q = \frac{1}{\rho} \eta \cdot \nabla \theta, \tag{1}$$

where q is PV, ρ is the air density, η is the absolute vorticity, θ is potential temperature, and ∇ is the three-dimensional nabla operator.

Here we use piecewise PV inversion based on nonlinear balance (Davis and Emanuel, 1991; Davis, 1992). Nonlinear balance (Charney, 1955) assumes that the wind's irrotational component is substantially smaller than the magnitude of the non-divergent wind (e.g., Davis, 1992; Seiler, 2019). Therefore, geopotential (Φ) as a function the non-divergent streamfunction (Ψ) and Ertel's PV can be expressed in spherical coordinates (Davis and Emanuel, 1991; Davis, 1992),

$$\nabla^2 \Phi = \nabla \cdot f \nabla \Psi + \frac{2}{a^4 \cos^2 \phi} \left[\frac{\partial^2 \Psi}{\partial \lambda^2} \frac{\partial^2 \Psi}{\partial \phi^2} - \left(\frac{\partial^2 \Psi}{\partial \lambda \partial \phi} \right)^2 \right] \tag{2}$$

and

$$q = \frac{g \kappa \pi}{p} \left[\left(f + \nabla^2 \Psi \right) \frac{\partial^2 \Phi}{\partial \pi^2} - \frac{1}{a^2 \cos^2 \phi} \frac{\partial^2 \Psi}{\partial \lambda \partial \pi} \frac{\partial^2 \Phi}{\partial \lambda \partial \pi} \right.$$
$$\left. - \frac{1}{a^2} \frac{\partial^2 \Psi}{\partial \phi \partial \pi} \frac{\partial^2 \Phi}{\partial \phi \partial \pi} \right], \tag{3}$$

respectively, where Φ is the geopotential, Ψ is the non-divergent streamfunction, λ is longitude, ϕ is latitude, a is the radius of the earth, $\kappa = R/C_p$ is the Poisson constant, f is the Coriolis parameter, p is pressure, and $\pi = (p/p_0)^\kappa$ is the Exner function.

Solving Eqs. (2) and (3) for the unknowns Φ and Ψ given q on a limited domain conduces to the full PV inversion (Davis and Emanuel, 1991). Regarding boundary conditions, Φ and Ψ are prescribed on the lateral domain boundaries (Dirichlet boundary conditions) and their vertical derivatives on the horizontal boundaries (Neumann boundary conditions). On the lateral boundaries, the observed geopotential is employed as the boundary condition for Φ and $\frac{\partial \Phi}{\partial \pi} = -\theta$ is used at the top and bottom of the domain (for more details see Davis, 1992).

At each grid point, PV anomalies are calculated as deviations from the PV background, defined here as a running mean over a 30 d time slice. A full PV inversion is computed for instantaneous values (q) and for 30 d mean values ($\overline{q}$), conducting to instantaneous balanced Φ and Ψ, as well as mean balanced $\overline{\Phi}$ and $\overline{\Psi}$.

The PV inversion is performed for the time of maximum intensity for each cyclone track and in a three-dimensional box bounded by the 900 and 100 hPa pressure surfaces, with a horizontal dimension of 15° latitude and 30° longitude around the cyclone center of interest. Furthermore, PV
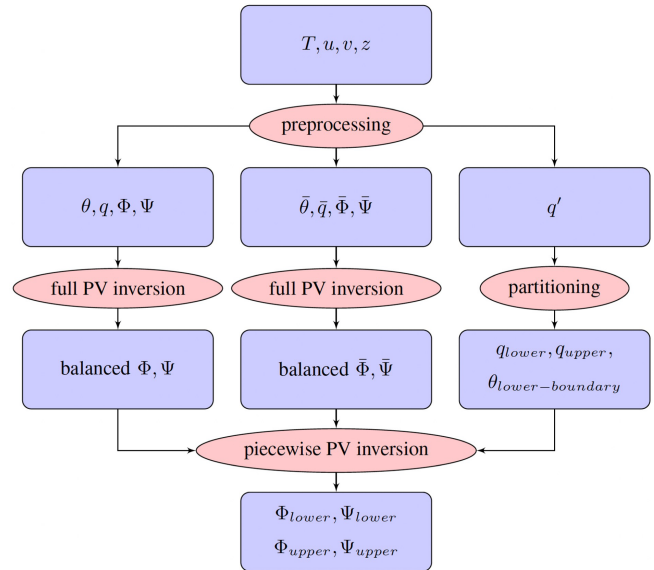

Figure 1. Algorithm for computing the piecewise potential vorticity inversion. Rectangles indicate variables, including temperature T, zonal wind speed u, meridional wind speed v, geopotential height z, potential vorticity q, geopotential Φ, and streamfunction Ψ, and ovals show steps of the calculation. Adapted from Seiler (2019).

anomalies q' in upper- and lower-tropospheric layers are considered separately from each other (right column in Fig. 1): the upper layer between 550 and 150 hPa, the lower layer between 850 and 600 hPa, and the lower boundary contribution at 875 hPa. Note that in the lower layer contribution, the PV anomalies and potential temperature at the boundary are separated, but the upper layer contribution contains both PV anomalies and temperature at the upper boundary. The separation level between these anomalies (600 hPa) is consistent with the transition of the shape of the PV features from lower to higher levels (see Fig. S2). See Fig. 1 for a general overview of the PPVI algorithm. The CESM-LE output is provided on hybrid sigma-pressure coordinates and, for the PPVI, is interpolated to equidistant isobaric levels ($\Delta P = 50$ hPa) between 1000 and 50 hPa. Furthermore, in regions of high topography, the data are extrapolated below the ground. Following Davis and Emanuel (1991), temperature is extrapolated using a constant lapse rate (moist), and then the geopotential is obtained by using the hydrostatic equation and state equation. Finally, the missing wind components (u, v) below the ground are filled by propagating the last value available downward.

Because of the computational effort, the piecewise PV inversion is not performed for all cyclones mentioned above (the strongest 10 %) but only for the strongest 1 % of cyclones, which are denoted as extreme cyclones in the following.

4   Results

4.1   Storm tracks

In order to provide an overview of the simulated cyclone climatology and put the following more specific results in context, this section describes the climatology of cyclones in the CESM-LE simulations in comparison with ERA-Interim data. Subsequently, projected changes in winter storm tracks and cyclone intensity in a warmer climate at the end of the century over the North Atlantic are presented.

Figure 2a shows the storm track density from ERA-Interim for the extended winter season (October–March). A region of high cyclone frequency extends from the East Coast of the USA to northern Europe. The cyclone density maximum is located to the south of Greenland. The Mediterranean region is another area with enhanced cyclone activity. This storm track distribution is similar to previous studies (e.g., Wernli and Schwierz, 2006; Ulbrich et al., 2009; Neu et al., 2013; Zappa et al., 2013).

The CESM-LE model bias for the winter months is shown in Fig. 2b. In general, in the North Atlantic basin, the model tends to produce more cyclones over the USA East Coast, between Iceland and Norway, around Greenland, over southern Spain, and over parts of eastern Europe. However, there is a predominant underestimation of cyclone frequencies over the ocean. These results are again similar to previous studies based on the CESM-LE model (e.g., Day et al., 2018; Raible et al., 2018). Nevertheless, the CESM-LE storm track is not oriented too zonally over the North Atlantic, which is in contrast to many CMIP5 climate models (see Zappa et al., 2013). For the interpretation of this bias, it is important to keep in mind that this analysis also includes weak cyclones, which may cause noisy results in some regions. This is particularly evident for the summer season (not shown).

Aggregated over the entire North Atlantic basin, CESM-LE reproduces cyclone frequencies and lifetimes fairly well (Fig. 2c), in particular of those cyclones with a lifetime of 6 d or more. The number of shorter-lived cyclones is slightly underestimated compared to ERA-Interim.

The cyclone activity response in a warmer climate at the end of the century [future (2091–2100) – present (1990–2000)] is particularly variable over the North Atlantic region (Fig. 3a). Despite this variability, there are some evident changes. The cyclone frequency decreases over the main storm track region, the USA East Coast, southern Greenland, and the Mediterranean region. Figure 3b indicates that this decrease is mainly related to cyclones with a short life of 2 d or less. A similar reduction in cyclone frequencies has been reported in other studies using the CESM-LE model (e.g., Day et al., 2018; Raible et al., 2018) and other CMIP5 models (Zappa et al., 2013). Figure 3a also indicates more substantial cyclone frequency changes at higher latitudes around Greenland, in particular an increase in cyclone frequency to the west and north of Greenland. A slight increase is also found north of the United Kingdom and west of the Scandinavian Peninsula. Zappa et al. (2013) show a more evident increase over the United Kingdom, based on their multi-model analysis, which is less evident in Fig. 3a. This difference may be due to a specific signature in CESM-LE. Nevertheless, it might also be related to differences in the cyclone tracking scheme and to the fact that we considered the months of October–March while Zappa et al. (2013) analyzed December–February. Also note that Zappa et al. (2013) used the Hodges scheme for cyclone identification and tracking (Hodges, 1999). The sensitivity of the climate change signal of the cyclones to the choice of the tracking method was analyzed in detail by Ulbrich et al. (2013).

As a measure of extratropical cyclone intensity, we use the relative vorticity at 850 hPa (RV850) averaged over a radius of 250 km around the location of the sea-level pressure minimum for each time step during cyclone lifetime. The spatial pattern of projected future changes in cyclone intensity is shown in Fig. 3c. Extratropical cyclones are projected to become less intense over the main storm track and the Mediterranean region but more intense over the Norwegian Sea, over northern Scandinavia, and to the west and north of Greenland. Also, over central Europe, there is an area of a slight increase in cyclone intensity. However, less than 8 of 10 ensemble members agree on the sign of this change.

Figure 3d shows the frequency distribution of cyclone intensity for the entire North Atlantic regions in present-day and future climate. The distributions are similar (no substantial change in cyclone intensity), and for most intensities, the frequency slightly decreases between present-day and future climate. There is only a subtle increase in the frequency of intense cyclones. The future-climate 90th percentile of cyclone intensity is close to its present-day value, but the 99th percentile increases in the future. The presence of stronger winter cyclones in a warming climate has been suggested by Zappa et al. (2013); however, this result is less evident in our analysis.

We also explore projected changes in the maximum wind speed related to extratropical cyclones. The maximum wind speed at 850 hPa is found in a radius of 500 km around the location of the sea-level pressure minimum for each time step during cyclone lifetime. Figure 3e and f show future changes in the spatial pattern and frequency distribution of the cyclone-associated maximum wind speed. The spatial patterns are similar to the changes in cyclone intensity (see again Fig. 3c) and generally tend to follow the cyclone track response, with an increase in cyclone intensity and maximum winds in regions where the cyclone frequency is projected to increase. However, increases in maximum wind speed (e.g., over central Europe) are typically more pronounced than the changes in cyclone intensity. An increase in maximum wind speed of more than 10 % is found north of the United Kingdom.

In summary, this section shows that the cyclone frequency biases in CESM-LE are relatively small in the main storm
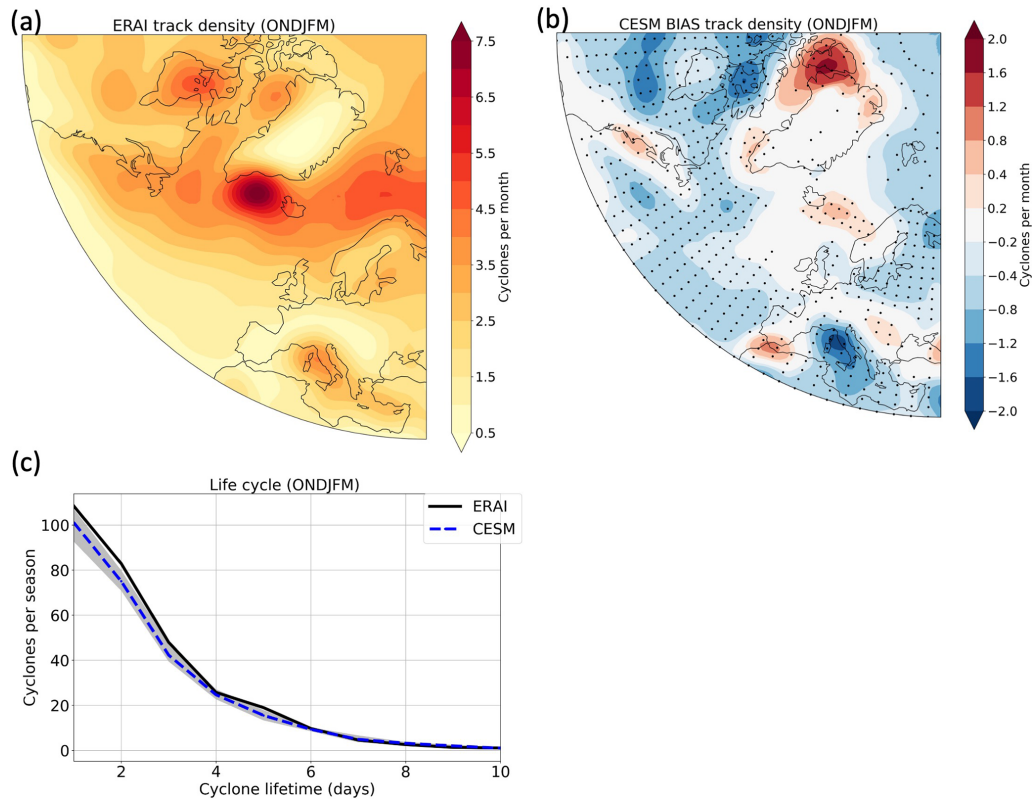
Figure 2. (a) Cyclone track density (number of cyclones per month per unit area) in ERA-Interim (1979–2010) over the North Atlantic for the extended winter season. **(b)** Mean track density bias of CESM-LE (1990–2000) relative to ERA-Interim (1979–2010). Black dots in panel **(b)** denote regions of ensemble agreement on the sign of bias; i.e., more than 80 % of the ensemble members indicate a bias of the same sign. **(c)** Statistical cyclone count as a function of cyclone lifetime in ERA-Interim (1979–2010) and CESM-LE (1990–2000) for the extended winter season in the North Atlantic region. Ensemble mean (blue dashed line) and spread of ensemble members 1–10 (grey color shading) are shown.

track region and are mainly due to short-lived cyclones. Future projections of cyclone frequencies mostly indicate a decrease over the ocean and the Mediterranean region, consistent with previous studies. Finally, cyclone intensities are not projected to change substantially overall, and the spatial variations in intensity changes are similar to frequency changes. This lack of major cyclone intensity changes is consistent with previous studies (Ulbrich et al., 2009; Zappa et al., 2013; Pfahl et al., 2015; Day et al., 2018; Raible et al., 2018) and most likely due to the competition between different thermodynamic and dynamic factors, as outlined in Sect. 1.

4.2 Composites of intense extratropical cyclones

In the previous section, we see that there are only minor projected changes in cyclone intensity in CESM-LE. However, even if overall intensity changes are small, there may be changes in cyclone dynamics and structure that can affect, e.g., spatial patterns of near-surface winds. Hence, we focus in more detail on the cyclone structure and dynamic properties in the following. The leading hypothesis is that changes in cyclone impacts, such as wind gusts, do not occur only be-

cause of the shift in storm tracks but also because the properties of individual cyclones may change in a warming climate. Therefore, this section aims to investigate storm-scale dynamical changes with the help of composite analysis.

For the composite analysis, we use the strongest 10 % of storms over the North Atlantic in each ensemble member. In this way, the focus is laid on the main storm track region over the ocean (as shown in Fig. 4a), where the model also has the smallest biases compared to other regions such as the Mediterranean. In addition, the strongest 10 % of cyclones are the most relevant ones in terms of wind impacts.

Figure 4b shows the future change in intense cyclone frequency. A bipolar pattern dominates the response in track density. An increase in intense cyclone frequency is projected over the northeast Atlantic region. The increase spreads over the northern United Kingdom and the western coast of Norway. In contrast, there is a reduction in track density to the south and east of Greenland. These results are again similar to the strong cyclone response found by Zappa et al. (2013), who defined strong cyclones as those exceeding a threshold in the maximum along-track wind speed at 850 hPa. How-
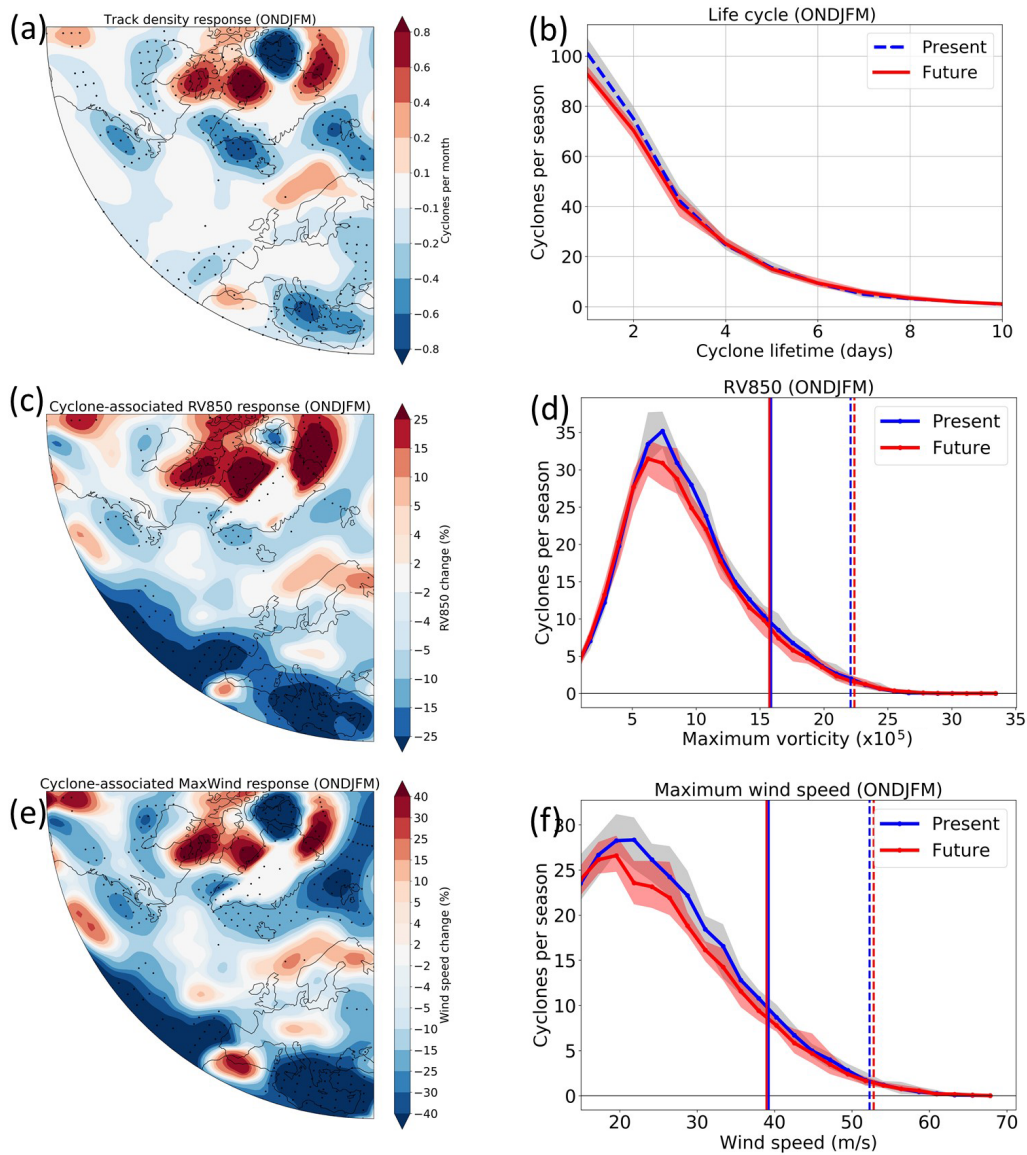
Figure 3. (a) Mean track density response [future (2091–2100) – present (1990–2000)] from CESM-LE in winter over the North Atlantic. **(b)** Statistical cyclone count as a function of lifetime in present-day and future-climate simulations. Ensemble mean (blue dashed line) and spread of ensemble members 1–10 (grey color shading) are shown. **(c)** Cyclone intensity response (%), measured in terms of averaged RV850. **(d)** Frequency distributions of cyclone intensity. **(e)** Response of cyclone maximum wind speed at 850 hPa (%). **(f)** Frequency distributions of cyclone maximum wind speed. The blue lines in panels **(d)** and **(f)** represent present-day climate (1990–2000), and the red lines represent future climate (2091–2100). The vertical lines show the 90th (solid) and 99th (dashed) percentiles, and the spread of ensemble members 1–10 is shaded. Black dots in panels **(a)**, **(c)**, and **(e)** denote regions of ensemble agreement on the sign of change; i.e., more than 80 % of the ensemble members indicate a change of the same sign.

ever, Fig. 4b indicates a more evident increase than the results shown by Zappa et al. (2013) in cyclone frequency in the eastern North Atlantic. Figure 4b also confirms that the notable changes in the frequency of all cyclones in Fig. 3a over west Greenland and high latitudes are due to relative weak storms.

Furthermore, the mean response found in the CESM model is also consistent with previous studies using single models (Leckebusch and Ulbrich, 2004; Pinto et al., 2009). For example, Pinto et al. (2009) analyzed the strongest 10 % of storms in the North Atlantic during the extended winter (October–March) with the ECHAM5 model and found an increase in cyclone frequency over the British Isles and the North Sea, but with the maximum increase slightly shifted southward in comparison to our results.
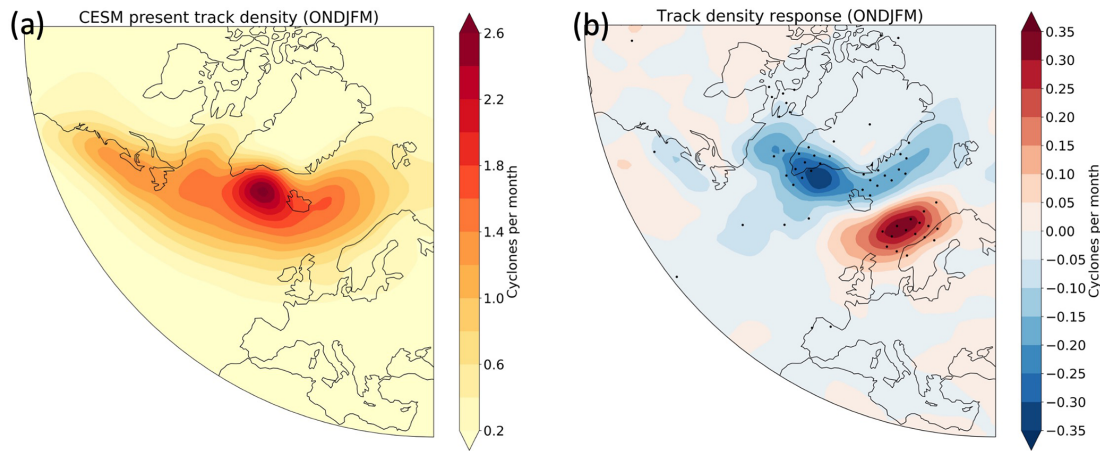
Figure 4. (a) Mean track density (1990–2000) of intense cyclones and **(b)** corresponding mean density response [future (2091–2100) – present (1990–2000)] from CESM-LE in winter over the North Atlantic. Intense cyclones are defined as the strongest 10 % of systems in terms of maximum RV850. Black dots in panel **(b)** denote regions of ensemble agreement on the sign of change; i.e., more than 80 % of the ensemble members indicate a change of the same sign.

Figure 5 shows the composites of relative vorticity at 850 hPa (RV850) and SLP (Fig. 5a), wind speed at lower levels (850 hPa, Fig. 5c), and wind speed at upper levels (250 hPa, Fig. 5e) for intense cyclones in present-day climate (1990–2000) at the time of their maximum intensity. RV850 (Fig. 5a) is largest in a region of approximately $\pm 2.5°$ around the cyclone center. The horizontal gradient of RV850 is larger upstream than downstream of the cyclone center. Therefore, high values of RV850 (values above $4 \times 10^{-5}\,\text{s}^{-1}$) cover a bigger area to the east of the SLP minimum, in the region of the warm front.

The wind speed at 850 hPa (Fig. 5c) shows a well-defined cyclonic circulation with equatorward flow upstream and poleward flow downstream of the cyclone center. The regional maximum in wind speed at 850 hPa is located to the southeast of the cyclone center, over the warm sector, where the highest values are above $26\,\text{m s}^{-1}$. Similar low-level wind patterns with the strongest winds in a region from southwest to east of the cyclone center have been found in previous studies (Slater et al., 2015, 2017). The wind speed maximum in Fig. 5c may be related to the low-level jet that typically occurs ahead of the cold front. This low-level jet and the associated wind shear can result in strong wind gusts at the surface (Lackmann, 2002). Note, however, that the compositing method may average out some of the airstream-related features. For instance, some storms may have the wind maximum behind the cold front associated with the cold conveyor belt and others in the low-level jet region ahead of the front, and averaging then produces a broader maximum covering the entire area.

The upper-level wind composite (Fig. 5e) shows the jet stream and its local maximum (jet streak) to the south of the cyclone center. The jet's wind direction is eastward to the south and poleward to the east of the cyclone center. The poleward flow to the east enhances the poleward motion of the low-level cyclone. Assuming that this poleward flow has also persisted in the period before maximum cyclone intensity, it may have contributed to cyclone intensification when the system crossed the upper-level jet axis (Rivière et al., 2013; Tamarin and Kaspi, 2017). At their time of maximum intensity, the most intense cyclones are typically located near the left exit region of the upper-level jet streak, as also evident from Fig. 5e, in an area of strong quasi-geostrophic forcing (Barnes and Colman, 1993; Deveson et al., 2002).

Changes in the composite patterns shown in Fig. 5b, d, and f are indicative of projected future changes in cyclone structure. The relative vorticity changes (Fig. 5b) have an intricate spatial pattern, with an RV850 reduction near the cyclone center and RV850 increases to the northeast and southwest of the SLP minimum. This may indicate enhanced relative vorticity values near the cold and warm fronts of intense cyclones in a warmer climate, as also suggested by Sinclair et al. (2020), who found a similar spatial pattern in aquaplanet simulations.

Figure 5d shows the wind speed changes at 850 hPa. A slight decrease in wind speed is projected north and northeast of the cyclone center, but in most other regions, wind velocities increase. The most significant increase emerges to the southeast of the center. This is related to a broadening of the footprint of strong winds (see again Fig. 5c) in the southeastward direction, further into the cyclones' warm sector. Similarly enhanced winds have been found in the new CMIP6 models (Priestley and Catto, 2021).

The wind speed changes at 250 hPa are shown in Fig. 5f. An increase in the wind velocity can be identified to the south and downstream of the cyclone center, linked to a more robust eastward flow and an enhanced jet stream. This increase is consistent with the mean response of the jet stream to en-
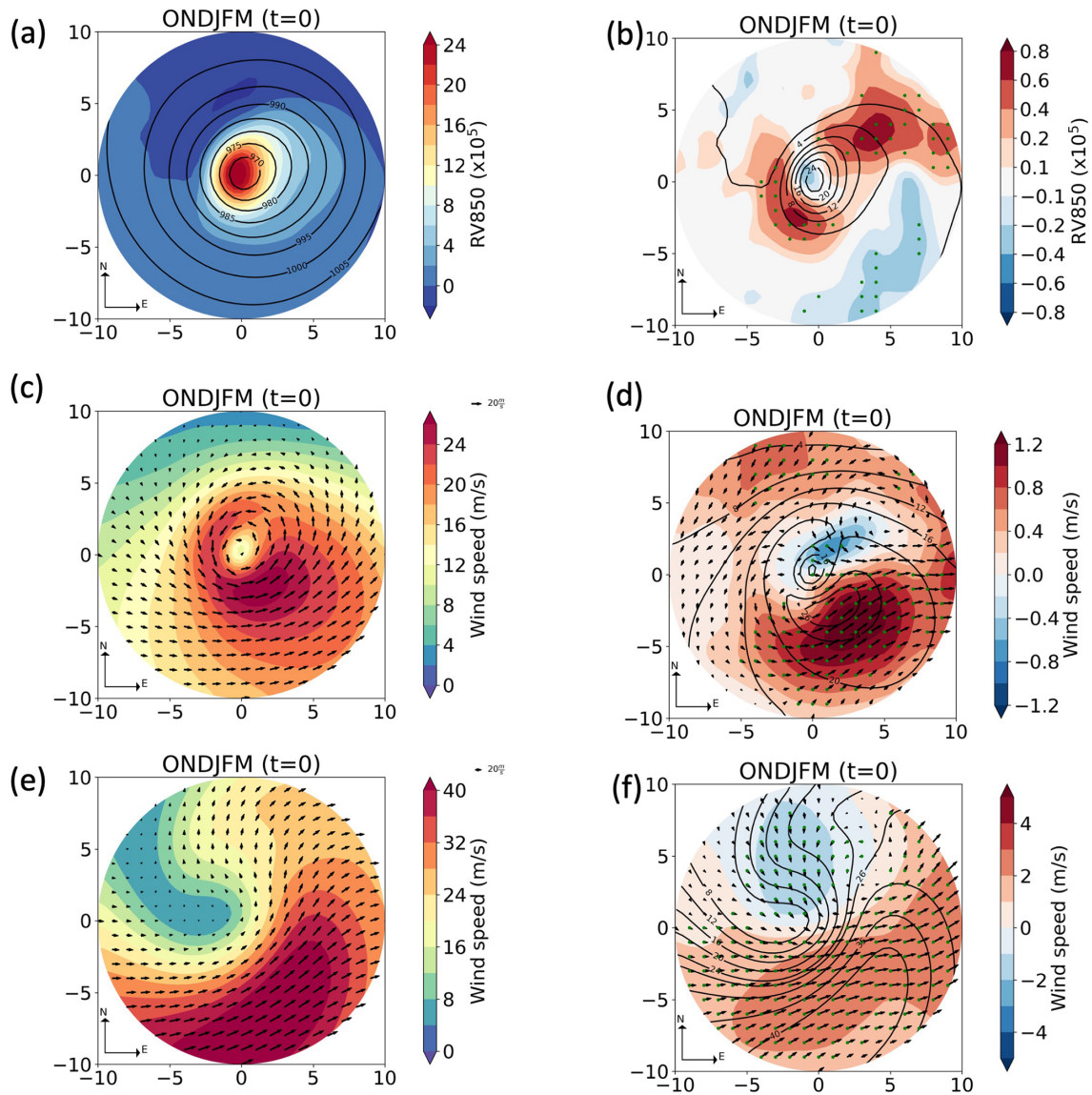
Figure 5. Present-day composites for intense cyclones of **(a)** relative vorticity, **(c)** wind speed at 850 hPa, and **(e)** wind speed at 250 hPa; panels **(b)**, **(d)**, and **(f)** show their future change for winter in the North Atlantic region. Mean SLP (hPa) is overlaid as black contour lines in panel **(a)**. The present-day mean of each field is overlaid as black contour lines in panels **(b)**, **(d)**, and **(f)**. Green dots in panels **(b)**, **(d)**, and **(f)** denote regions of ensemble agreement on the sign of change; i.e., more than 80 % of the ensemble members indicate a future change of the same sign. The composites are shown at the time of maximum intensity (time = 0).

hanced upper-tropospheric meridional temperature gradients (Grise and Polvani, 2014; Shaw et al., 2016; Priestley and Catto, 2021). Note that, at low levels, the wind increases are more robust than the decreases across the ensemble members (see the green dots in Fig. 5d), which might be due to small shifts in the location of the negative anomaly between ensemble members.

In the following, in order to better understand the changes in cyclone dynamics that are related to these altered wind patterns, we investigate composite potential vorticity anomalies and their projected future changes.

4.3 PV analysis

To first quantify simulated PV changes averaged over the cyclone area, Fig. 6 shows the PV anomaly profiles for intense cyclones in the North Atlantic region. At the time of maximum intensity ($t = 0$, Fig. 6b), there are prominent positive PV anomalies in the lower and upper troposphere, as typically associated with intense extratropical cyclones (Grams et al., 2011; Čampa and Wernli, 2012; Pfahl et al., 2015; Büeler and Pfahl, 2017). The lower-tropospheric PV anomaly is primarily created by diabatic processes, such
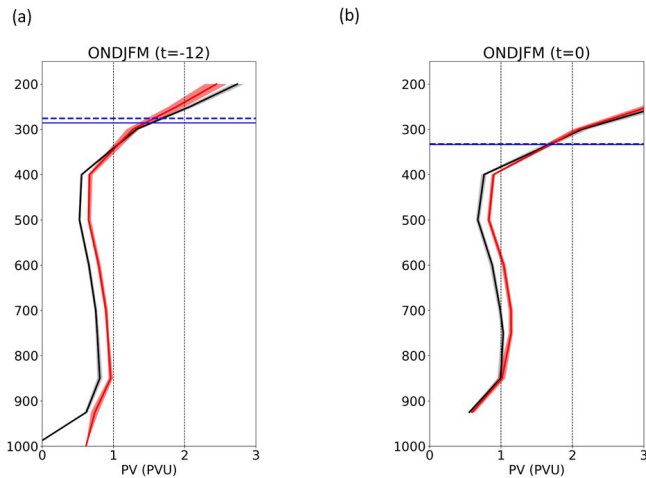
Figure 6. Vertical profiles of PV anomalies associated with intense extratropical cyclones in the North Atlantic region during winter for present-day climate (1990–2000), shown as black lines, and future climate (2091–2100), shown as red lines. Anomalies are calculated with respect to a local PV climatology and averaged in a radius of 2.5° around the cyclone center. The solid blue lines indicate the 2 PVU tropopause in the presence of cyclones for present-day (solid line) and future (dashed line) climate. Composite profiles are shown 12 h before **(a)** and at the time of maximum intensity **(b)**.

as latent heat released during cloud formation (Wernli and Davies, 1997; Ahmadi-Givi et al., 2004; Büeler and Pfahl, 2017). The upper-tropospheric PV anomaly is associated with adiabatic PV advection from the stratosphere and partly influenced by the cyclonic wind field linked to the lower-tropospheric PV anomaly (Hoskins et al., 1985; Wernli et al., 2002). Figure 6a shows the PV anomaly profile 12 h before the time of maximum intensity when both PV anomalies are still weaker and the low-level maximum is located at a higher pressure. As indicated by the blue lines in Fig. 6, the growth of the upper-tropospheric PV anomaly between $t = -12$ and $t = 0$ goes along with a lowering of the dynamical tropopause.

As a response to climate warming, at the time of maximum intensity ($t = 0$, Fig. 6b), there is a general increase in the lower and mid-tropospheric PV anomaly and a slight decrease in the upper-tropospheric PV anomaly. Note that the limited change in the upper-level anomaly is related to the relatively small averaging radius of 2.5°. Changes in the upper-level PV structure will become more evident in the composites discussed below. The amplification of the lower tropospheric PV anomaly is more robust in the layer between 850 and 600 hPa. These structural changes are similar to the previous finding of Büeler and Pfahl (2019) for intense cyclones based on idealized model simulations. For instance, also in these idealized simulations, the lower tropospheric PV maximum extends more into the middle troposphere in warmer climates. However, the magnitude of PV changes in the Büeler and Pfahl (2019) experiments is more prominent

than in the CESM-LE simulations presented here, which is mainly due to the fact that the range of climate warming is much more extensive in the idealized simulations.

The positive PV anomaly in the lowest part of the troposphere (below 850 hPa) increases more in the hours before maximum intensity (Fig. 6a). This increase is likely related to a more considerable influence of cloud formation and precipitation processes prior to the maximum intensity (Pfahl and Sprenger, 2016), which agrees with an analysis of the precipitation life cycle that will be presented in the second part of this study.

Finally, Fig. 6 indicates that the height of the tropopause during the presence of intense cyclones is projected to slightly increase, which reflects the general increase in tropospheric depth in a warming climate (O'Gorman and Schneider, 2008; Pfahl et al., 2015). This increase is more evident 12 h before the maximum intensity.

In the following, the horizontal structure of cyclone-related PV anomalies is also analyzed with the help of composites. Note again that a PV climatology specific to the respective climate (present-day vs future) has been subtracted from the full PV fields to obtain these anomalies. As shown in Fig. 7a, there is a clear, diabatically created maximum in the PV anomaly at 700 hPa near the cyclone center, which extends downstream in the region of the warm front. A secondary maximum can be observed along the northwestern flank of the composite region. The second maximum is likely related to frictional PV generation over the land masses such as Greenland and North America that are located to the northwest of the North Atlantic storm track (see again Fig. 4a).

The upper-tropospheric PV anomaly shown in Fig. 7c shows a dipole pattern, with high PV values associated with an upstream trough in the western part of the composite and a maximum southwest of the cyclone center. A clear signature of cyclonic wave breaking can be observed, which is also linked to the formation of the jet streak (see again Fig. 5e). This PV anomaly pattern is typical for extratropical cyclones during their mature stage of development (Pinto et al., 2014; Houze , 2014; Michaelis et al., 2017). Also, it is a signature of the deepening processes of the upper troposphere, which lead eventually to the "treble clef" upper-level PV (UPV) distribution characteristic of a warm-occluded structure in the lower troposphere (Martin, 1998).

Future changes of lower-tropospheric composite PV anomalies are shown in Fig. 7b. Positive PV anomalies are projected to increase in the region of the present-day maximum, near the cyclone center, but also downstream in the region of the warm front and generally in the area of the cyclone's warm sector. This increase is consistent with an increase in precipitation over the warm sector (as will be analyzed in more detail in another study) and with the overall rise of atmospheric moisture content, (cyclone) precipitation, and thus latent heat release in a warmer climate (Schneider et al., 2010; Yettella and Kay, 2017). Similar increases in lower-tropospheric PV have been found in other studies
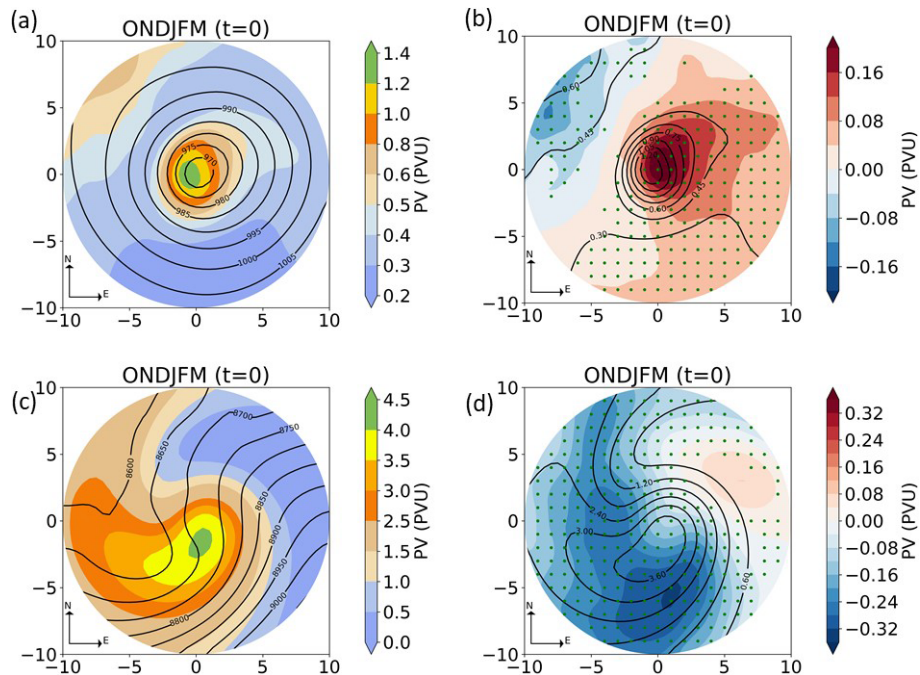
Figure 7. Present-day composites for intense cyclones of **(a)** PV at 700 hPa and **(c)** PV at 250 hPa and **(b, d)** their future change for winter in the North Atlantic region. Mean SLP (hPa) is overlaid as black contour lines in panel **(a)**, and geopotential height (m) is overlaid as black contour lines in panel **(c)**. The present-day mean of each field is overlaid as black contour lines in panels **(b)** and **(d)**. Green dots in panels **(b)** and **(d)** denote regions of ensemble agreement on the sign of change; i.e., more than 80 % of the ensemble members indicate a future change of the same sign. The composites are shown at the time of maximum intensity (time = 0).

(e.g., Marciano et al., 2015; Michaelis et al., 2017; Zhang and Colle, 2018; Sinclair et al., 2020) and have been directly attributed to enhanced latent heat release in idealized simulations (Büeler and Pfahl, 2019). Increased diabatic PV production in the region of the cold front may strengthen the low-level jet (Michaelis et al., 2017) (Fig. 5d), which is, however, difficult to detect in our PV composites as the cold front positions of different cyclones are not aligned. The increase in lower-tropospheric PV over the warm sector corresponds with an increase in relative vorticity (cf. Fig. 5b) in some areas, such as near the warm front, but not everywhere, pointing towards a complex relationship between PV and wind changes that will be further discussed below. Finally, PV at 700 hPa is projected to decrease in the region of the secondary maximum at the northwestern edge of the composite. This might be related to the eastward shift of the intense cyclone tracks in the northeastern Atlantic (see again Fig. 4b), which brings them further away from Greenland's topography.

The upper-level PV anomaly is projected to decrease in most regions but in particular upstream and south of the cyclone center (Fig. 7d). The most substantial reduction occurs along the southern flank of the PV maximum, pointing to a decreased wave breaking. A small PV increase is found downstream of the cyclone center, which is, however, hardly consistent across the ensemble member.

A similar reduction of upper-tropospheric PV has been found by Michaelis et al. (2017, their Fig. 7i). Parts of the PV decrease may be explained by changes in meridional PV advection. For instance, the slight increase in southerly upper-level wind velocities over the warm sector (see again Fig. 5f) may go along with enhanced advection of low-PV air masses from lower latitudes. In addition, an upward shift of the dynamical tropopause might contribute to such a PV decrease, although this tropopause shift is very small in the cyclones investigated here (see again Fig. 6) and thus not sufficient to explain the entire PV decrease. Finally, also enhanced LH at lower levels may impact the upper-level PV distribution through amplified upward motion and negative diabatic PV tendencies above the level of maximum heating. Michaelis et al. (2017) showed that this might lead to negative PV changes northeast of the cyclone center prior to (but not at) the time of maximum cyclone intensity. We will investigate the complex interplay between diabatic PV changes and PV advection (see also Brennan et al., 2008; Madonna et al., 2014) in the second part of this study using a Lagrangian approach.

The enhanced diabatic heating in a warmer and therefore more humid climate may thus influence PV anomalies and cyclone dynamics at both lower and upper levels. At low levels, it generates sizeable positive PV anomalies that directly contribute to cyclone intensification. This qualitative discus-

sion will be complemented by quantitative PPVI results be-
low.

Due to the relatively high computational effort, PPVI is not
performed for all intense cyclones, but only the strongest 1 %
of cyclones in the 10 ensemble members are analyzed, which
are referred to as extreme cyclones here. In this way, the fo-
cus is laid even more on the strongest storms with potentially
largest impacts in terms of near-surface wind velocities. Be-
fore we show the PPVI results, we thus briefly discuss com-
posite PV and wind changes associated with these extreme
cyclones.

In the lower troposphere, the future changes in PV and
wind composites of extreme cyclones (Fig. 8a, b) reproduce
the main features of the corresponding composite changes
of intense cyclones (cf. Figs. 7b and 5d), in particular re-
garding the regions of PV and wind speed increases that
are consistent across ensemble members. Nevertheless, dif-
ferences between extreme and intense cyclones are found in
the magnitude of changes. For example, the wind magnitude
increases by up to $1.2\,\mathrm{m\,s^{-1}}$ for intense cyclones, but by up
to $2.5\,\mathrm{m\,s^{-1}}$ for extreme cyclones. In addition, the region of
strong wind increase reaches further to the southeast for ex-
treme cyclones; i.e., the wind footprint is even further en-
larged, and there is a stronger poleward component in the
wind change for extreme cyclones. Also, the maximum mag-
nitude of (diabatic) PV changes is about twice as large for
the extreme as for the intense cyclones. These results further
support the hypothesis that the strengthening of the low-level
winds can be associated with diabatic potential vorticity in-
crease: a larger amplification of diabatic PV generation in
extreme cyclones goes along with a larger increase also in
wind speed.

In contrast to the lower troposphere, upper-level PV
changes for extreme cyclones differ more substantially from
those for intense cyclone. For instance, Fig. 8c indicates an
upper-level PV increase near the cyclone center, where a
decrease is projected for intense cyclones (Fig. 7d). How-
ever, this increase is not robust across ensemble members.
A PV reduction to the south and west of the cyclone center,
on the other hand, is common to both extreme and intense
cyclones. Upper-level wind speed changes for extreme cy-
clones (Fig. 8d) again follow a similar spatial pattern as for
intense cyclones (Fig. 5f) with amplified magnitude. Similar
to the lower levels, the wind change in the region of the main
jet has a more pronounced poleward component in extreme
cyclones.

Altogether, this comparison indicates that, at lower lev-
els and with regard to upper-level winds, changes in extreme
cyclones are qualitatively similar to changes in intense cy-
clones. There are some differences in the behavior of the
two cyclone classes in terms of projected upper-level PV
changes, which can, however, be partially attributed to nat-
ural climate variability (as they are not robust across the en-
semble of model simulations).

4.4   PPVI analysis of extreme extratropical cyclones

A piecewise inversion is performed to quantify the relative
contributions of upper- and lower-level PV anomalies to pro-
jected future wind speed changes in extreme cyclones and
thus complement the previous qualitative discussion. The
usefulness of such an inversion method to explain wind
changes has been demonstrated in previous studies (e.g.,
Tochimoto and Niino, 2016; Tamarin-Brodsky and Kaspi,
2017).

As described in Sect. 3.3, the PPVI separates the tropo-
sphere into an upper and a lower layer, and the effect of
PV anomalies in each layer is separately evaluated. Figure 9
shows PV composites averaged over these layers. The spatial
distribution shows a clear difference between the upper and
lower layers. The lower layer is characterized by a localized
PV anomaly in the region of the cyclone center, similar to the
PV anomaly composite at 700 hPa for extreme cyclones (see
again Fig. 8a). In contrast, the average upper-layer anomaly
has a broader maximum southwest of the center and a cy-
clonic wave-breaking structure, reminiscent of the extreme
cyclone anomaly at 250 hPa (Fig. 8c). Thus, the chosen sep-
aration level at 600 hPa appears to work well in separating
these different structures (for more details, see Fig. S2). Fig-
ure 9b and d also show the future changes of the layer-mean
PV anomaly composites. These projected changes are again
consistent with our previous findings for specific levels (see
Fig. 8). The lower-tropospheric anomaly increases mostly
near the cyclone center and in the region of the fronts. In
the upper layer, there is a reduction of PV to the south of
the cyclone center and a PV increase near the center. Fig-
ure 9e shows the temperature anomalies at the lower bound-
ary in present-day climate. A predominant positive anomaly
is found downstream and a negative anomaly upstream of the
cyclone center. Future changes (Fig. 9f) are characterized by
a temperature anomaly reduction to the north of the cyclone
center and two regions of increased temperature to the west
and southeast of the cyclone center. The latter (the most sig-
nificant increase) covers most of the warm sector. Figure 8b
shows a southward wind response to the north of the cyclone
center as the climate warms and stronger southwesterlies in
the warm sector. The temperature anomalies in Fig. 9f can
thus be related to amplified cold air advection north and am-
plified warm air advection southeast of the cyclone center.

Figure 10 shows the results of the PPVI for wind speed
composites at 850 hPa in present-day climate (upper row)
and their projected future change (lower row). The bal-
anced wind composite (Fig. 10a) is obtained from inverting
the complete PV distribution in the specified domain (see
again Sect. 3.3 for more details). It is broadly similar to the
full wind composite (present-day composites for extremes,
Fig. S3a), the wind speed increases southward, and there is
a band of strong winds upstream. Nevertheless, the balanced
wind speed has a smaller magnitude over the cyclones' warm
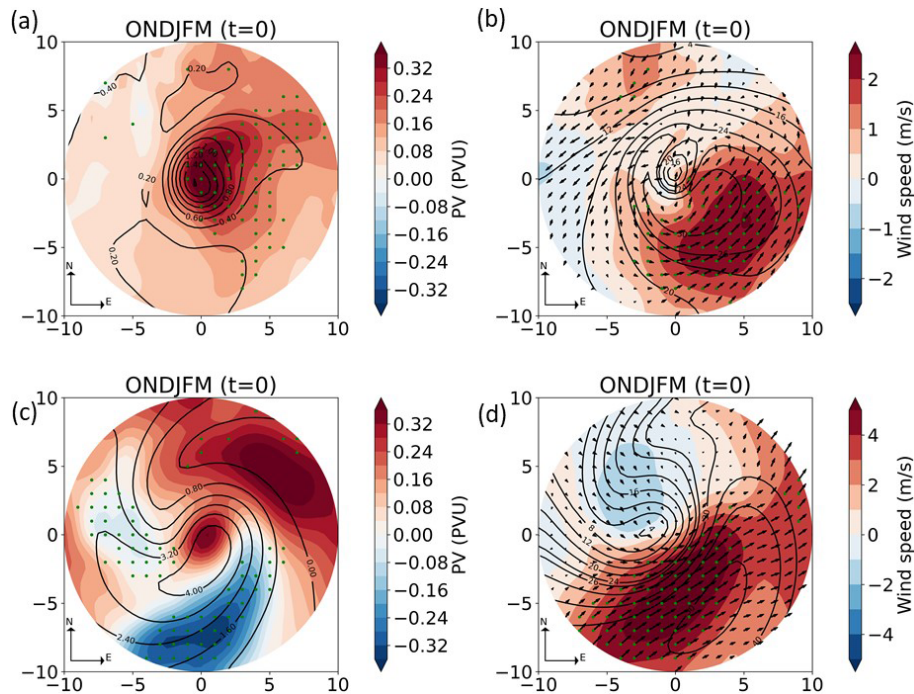sector. This indicates that the high winds in this region, which

Figure 8. Future change in composites for extreme cyclones of **(a)** PV at 700 hPa, **(b)** wind speed at 850 hPa, **(c)** PV at 250 hPa, and **(d)** wind speed at 250 hPa for winter in the North Atlantic region. The present-day mean of each field is overlaid as black contour lines. Green dots denote regions of ensemble agreement on the sign of change; i.e., more than 80 % of the ensemble members indicate a future change of the same sign. The composites are shown at the time of maximum intensity (time = 0). Extreme cyclones are defined as the strongest 1 % of systems in terms of maximum RV850.

are partly associated with the low-level jet ahead of the cold front, have an essential non-balanced component (divergent component).

Also, projected future changes in the balanced wind (Fig. 10e) reproduce changes in the full wind (Fig. 8b) fairly well, although they are less consistent between the different ensemble members. In particular, they also show increased wind velocities and an extended wind footprint in the warm sector. PPVI allows for a decomposition of the balanced flow and its changes into contributions from different anomalies, here the upper- and lower-layer PV anomalies, temperature anomalies at the lower boundary as well as the background PV field. For the 850 hPa winds, the background only has a small contribution (see Fig. S4).

Figure S6, a comparison between the balanced flow and the sum of the total contributions, demonstrates the consistency of this decomposition and shows that both the present-day balanced flow and its projected change are similar to the sum of the individual contributions. Differences between the balanced flow and the sum of all wind components arise due to (i) the imperfect knowledge of boundary conditions; (ii) non-linearities associated with the separation, especially the separation of low-level temperature anomalies and low-level PV anomalies; and (iii) numerical inaccuracies, mostly in calculating the Neumann boundary condition at 125 hPa, where the vertical θ gradient is very large.

The decomposition of the present-day wind composite (Fig. 10a–d) indicates that all three anomalies contribute to the cyclonic circulation. The weakest contribution comes from the temperature anomaly, whose center of circulation is also shifted northwestward compared to the cyclone center. The upper-layer PV anomaly has overall the largest contribution, in particular for the poleward flow downstream of the cyclone center, where the horizontal PV gradients in the upper layer are also the largest (cf. Fig. 9c). Low-layer PV contributes most substantially to the equatorward flow upstream of the center, again in the region of largest low-layer PV gradients. The critical role of upper-layer PV for the flow at 850 hPa seen in Fig. 10 is generally consistent with our conceptual understanding of cyclone intensification (Hoskins et al., 1985) and with previous PPVI results (Seiler, 2019).

The future change of PPVI decomposition of the wind flow at 850 hPa is discussed now. The largest contribution to the future changes in balanced flow at 850 hPa (Fig. 10e) is associated with low-layer PV changes (Fig. 10h). The increase in low-layer PV at the cyclone center (cf. Fig. 9b), which is mainly due to enhanced latent heating (see again Sect. 4.3), is linked to amplified cyclonic circulation all around the cyclone center but in particular to its west, where the already strong PV gradients are further enhanced. However, this amplification of the equatorward flow upstream is partly compensated for by a reduced equatorward component (Fig. 10f)
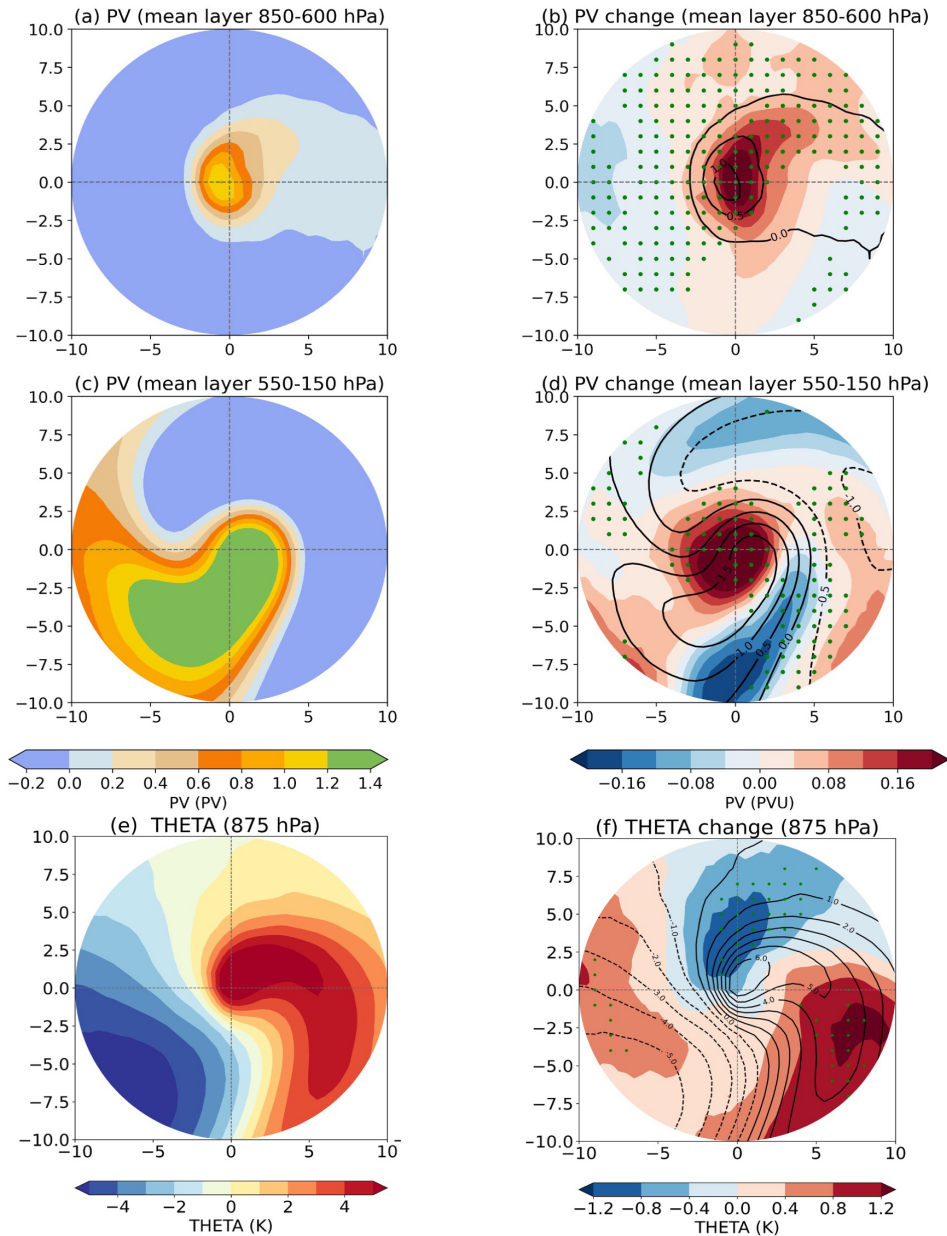
Figure 9. Present-day composites for extreme cyclones of PV averaged over **(a)** the lower troposphere (850–600 hPa), **(c)** the upper troposphere (550–150 hPa), and potential temperature at 875 hPa (lower boundary) for winter in the North Atlantic region. Future changes of the lower tropospheric PV, upper tropospheric PV, and potential temperature are shown in panels **(b)**, **(d)**, and **(f)** respectively. The present-day mean of each field is overlaid as black contour lines in panels **(b)**, **(d)**, and **(f)**. Green dots in panels **(b)** and **(d)** denote regions of ensemble agreement on the sign of change; i.e., more than 80 % of the ensemble members indicate a future change of the same sign. The composites are shown at the time of maximum intensity (time = 0).

associated with a reduction in the upper-layer PV gradient due to a PV increase to the northwest of the present-day maximum (Fig. 9d). In contrast, in the warm sector southeast of the cyclone center, both changes in lower- and upper-layer PV are associated with an enhanced southwesterly flow and thus add up to produce higher wind velocities and an enlarged wind footprint (see again Fig. 10e). This wind speed increase in the warm sector is slightly reduced by changes

in the temperature anomaly at the lower boundary that are linked to an anomalous anti-cyclonic circulation centered northwest of the cyclone center (Fig. 10g). The anti-cyclonic circulation is located over a cold anomaly (Fig. 9f). Altogether, these results show that the projected enhancement of the wind footprint in the warm sector cannot be attributed to a single mechanism alone but results from a constructive
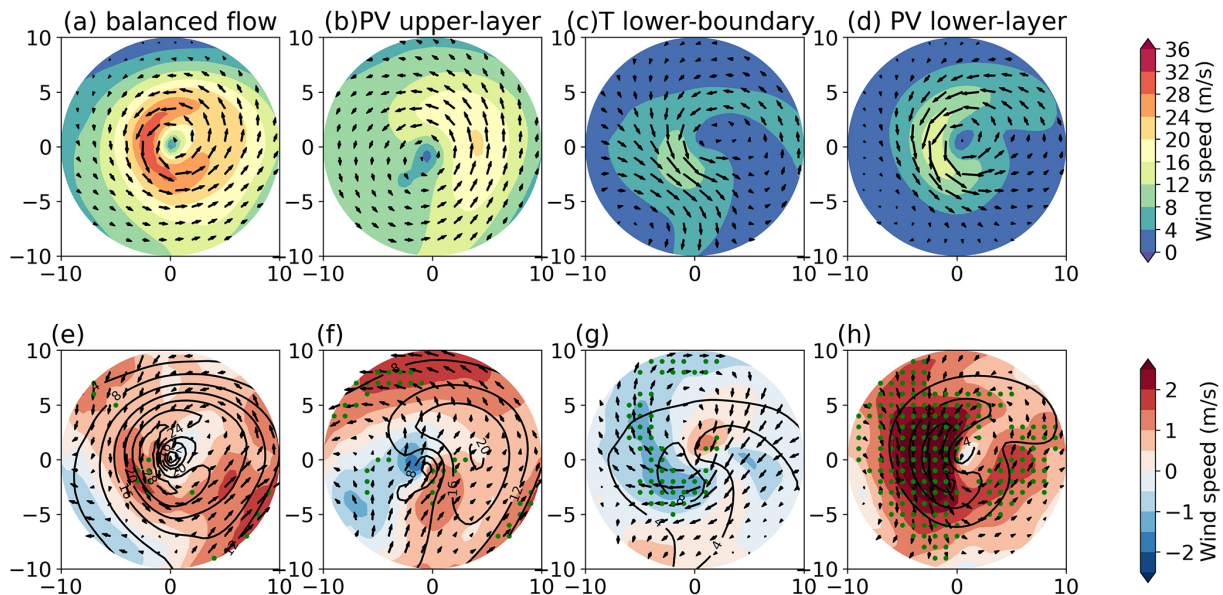
Figure 10. PPVI decomposition of the wind composites at 850 hPa in present-day climate (upper row) and their future change (lower row). The total balanced wind composite obtained from the full PV inversion is shown in panels **(a)** and **(e)**. The other panels show the wind composites obtained from inverting **(b, f)** the upper-layer PV anomalies, **(c, g)** temperature anomalies at the lower boundary, and **(d, h)** the lower-layer PV anomalies. Green dots in panels **(b)** and **(d)** denote regions of ensemble agreement on the sign of change; i.e., more than 80 % of the ensemble members indicate a future change of the same sign.

superposition of wind changes linked to upper- and lower-tropospheric PV anomalies.

Also, for wind speed in the upper troposphere, at 250 hPa (Fig. 11), the balanced flow from the PV inversion reproduces the present-day wind composite (cf. Fig. S3b) and its projected future change (cf. Fig. 8d) qualitatively. However, the present-day wind velocities are underestimated (Fig. 11a), and the small projected wind speed reduction northwest of the cyclone center (which is not consistent across ensemble members) is not captured (Fig. 11d). As for the low-level wind, the PPVI yields a consistent decomposition of this balanced flow and its future change (Fig. S7). Nevertheless, the contributions of low-layer PV and temperature anomalies at the lower boundary are small (see Fig. S5), such that only contributions of upper-layer PV and the background flow are shown in Fig. 11.

The present-day wind composite at 250 hPa (Fig. 11a) is a superposition of westerly background flow with a wind speed maximum at the southern edge of the domain (Fig. 11c) and a component linked to the upper-layer PV anomaly (Fig. 11b), which is mostly poleward to the east and westward to the west of the cyclone center.

The future wind speed increase at upper levels, which is mostly found to the south and east of the cyclone center (Fig. 11d), results from a combination of the two mentioned components: first, an amplified westerly background flow (Fig. 11f), consistent with previous studies of future changes in the upper-level jet (Grise and Polvani, 2014; Shaw et al., 2016); and, second, the larger wind velocities linked

to upper-layer PV changes (Fig. 11e). The latter is most prominent in a region of enhanced PV gradients associated with the dipole pattern of projected PV changes (see again Fig. 9d) southeast as well as north of the cyclone center. Similar patterns of upper-level wind speed changes in mid-latitude cyclones have been found by Tamarin-Brodsky and Kaspi (2017). The enhanced poleward flow is thought to contribute to the increased poleward propagation of cyclones in a warmer climate (Tamarin-Brodsky and Kaspi, 2017) and, as discussed in Sect. 4.3, can feed back on the PV anomaly pattern by transporting low-PV air masses from lower latitudes towards the cyclone center.

5 Conclusions

In this study, an analysis of cyclone dynamics and wind changes in a warming climate has been performed with the help of coupled climate model simulations and a potential vorticity framework. A cyclone tracking scheme and composite and PV inversion diagnostics have been applied to 10 CESM-LE ensemble members. The model reproduces cyclone frequencies over the North Atlantic well, in particular over the main storm track regions. Model biases are mostly associated with the representation of short-lived systems.

At the end of the century, projected changes in cyclone frequencies are relatively small, with a general tendency towards slight decreases in many regions. Nevertheless, for the 10 % most intense cyclones, an eastward displacement
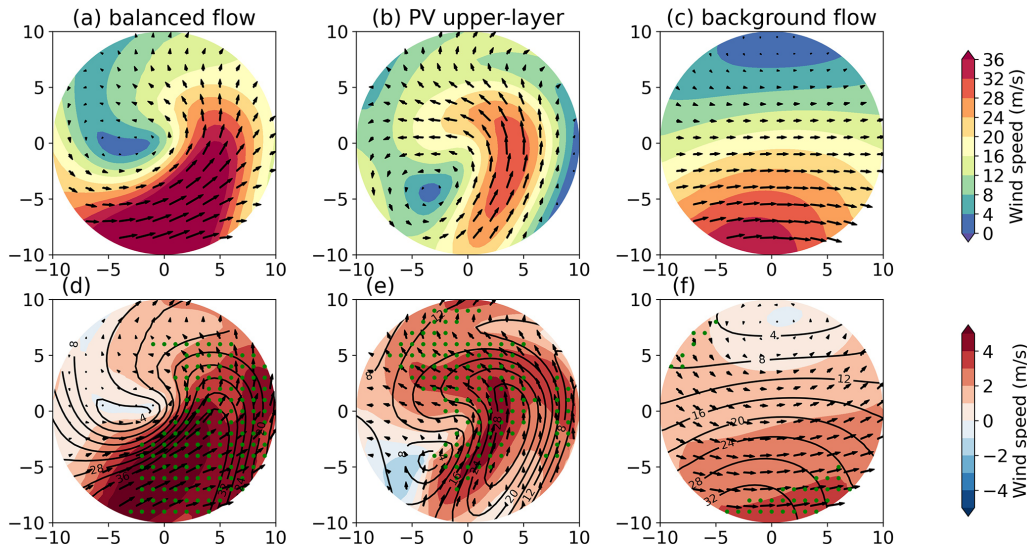
Figure 11. PPVI decomposition of the wind composites at 250 hPa in present-day climate (upper row) and their future change (lower row). The total balanced wind composite obtained from the full PV inversion is shown in panels **(a)** and **(d)**. The other panels show the wind composites obtained from inverting **(b, e)** the upper-layer PV anomalies and **(c, f)** the background PV. Green dots in panels **(b)** and **(d)** denote regions of ensemble agreement on the sign of change; i.e., more than 80 % of the ensemble members indicate a future change of the same sign.

of the main oceanic storm track over the eastern North Atlantic is projected, associated with an increase in cyclone track density over northwestern Europe. These findings on cyclone frequency changes are generally consistent with previous studies using other climate models and cyclone tracking approaches (Pinto et al., 2009; Ulbrich et al., 2009; Zappa et al., 2013). Also, projected cyclone intensity changes, measured in terms of lower-tropospheric maximum relative vorticity or wind speed, are relatively small, again consistent with previous studies (Zappa et al., 2013; Catto et al., 2019).

In spite of such small overall intensity changes, our composite analysis indicates structural changes in the typical wind patterns associated with intense North Atlantic cyclones. In particular, an increase in wind velocities in the warm sector southeast of the cyclone center, potentially related to strengthening the low-level jet ahead of the cold front, and a southeastward broadening of the associated footprint of strong winds are projected. While some previous studies on future wind changes in cyclones have not detected such a robust change (Michaelis et al., 2017), consistent results regarding the broadening wind footprint have been obtained from idealized simulations (Sinclair et al., 2020) and a recent analysis of CMIP6 model projections (Priestley and Catto, 2021). Together with the eastward shift of storm tracks, this may lead to increased wind hazards in western Europe, which has also been seen in other model studies (Mölter et al., 2016).

In order to better understand the dynamical mechanisms behind these wind speed changes, a PV anomaly and inversion analysis has been conducted. PV inversion has been used previously to study future changes in cyclone propagation (Tamarin-Brodsky and Kaspi, 2017; Tamarin and Kaspi, 2017), but here it has been used for the first time for the investigation of future changes in the near-surface wind patterns associated with midlatitude cyclones. In agreement with many previous studies (Pfahl et al., 2015; Marciano et al., 2015; Michaelis et al., 2017; Zhang and Colle, 2018; Sinclair et al., 2020), we find an increase in lower-tropospheric PV near the cyclone center and fronts that is most likely due to increased latent heating in a warmer and thus more humid climate (Büeler and Pfahl, 2019).

According to our PPVI analysis, this amplified low-level PV is associated with enhanced cyclonic wind velocities around the cyclone center, indicating that the increased latent heating contributes to the broadening of the wind footprint in the warm sector. However, it is not the sole cause of this broadening, as also PV changes in the upper troposphere go along with an increase in southwesterly winds in this region. More specifically, a dipole change in upper-tropospheric PV with a projected PV increase near the cyclone center and a decrease to the south and southwest are associated with enhanced upper-level PV gradients in the region ahead of the cold front and thus increased poleward flow throughout the troposphere. In contrast to the warm region southeast of the cyclone center, where wind changes associated with upper- and lower-layer PV changes superimpose in a constructive way, these wind changes partly compensate for each other upstream of the cyclone center, where net wind speed changes are thus smaller. Note that the projected wind increase in the warm sector is robust across the different cy-

clone intensity classes and ensemble members analyzed here and is also seen in the balanced wind response of the PV inversion. However, the PPVI does not exactly reproduce the full wind changes in a quantitative way, and the corresponding results should thus be interpreted with care.

The analysis presented here has some limitations. It is based on a single climate model and thus does not take model uncertainty into account. On the other hand, by using several ensemble members, we have assessed the robustness of our findings with respect to natural climate variability (similar to, e.g., Yettella and Kay, 2017). Furthermore, our study uses a single cyclone tracking algorithm, which has been applied successfully before in many other studies on midlatitude cyclones (e.g., Pfahl et al., 2015; Sprenger et al., 2017) and gives results that are in the range of other tracking schemes (Neu et al., 2013). Arguments for the robustness of our findings with respect to this choice of the tracking scheme are, again, that similar results have been obtained with other tracking algorithms, also using the same climate model (Day et al., 2018), and that the dependence on the tracking scheme is generally weaker for intense (compared to weak) cyclones (Neu et al., 2013; Ulbrich et al., 2013). Our results have been presented on specific vertical levels but are generally robust with respect to small shifts of these levels (see for instance Figs. 8 and 9). Finally, as discussed in Sect. 4.4, the PV inversion results can be affected by errors due to imperfect knowledge of boundary conditions, non-linearities, and numerical inaccuracies. Especially the separation between low-level PV anomalies and lower boundary θ-anomalies is affected by such errors, since the far-field impact of the low-level PV anomalies onto potential temperature below is not known. Nevertheless, we have shown that the associated residuum of the decomposition is relatively small and that the inversion method is able to reproduce the main features of the projected wind changes.

In summary, the PV analysis performed in this study provides insights into the role of altered upper-tropospheric dynamics and increased latent heat release in a warmer climate for future changes in near-surface wind fields around extratropical cyclones. The projected broadening of the wind footprint southeast of the cyclone center that can be explained by a combination of these processes may have important consequences for future changes in wind hazards. This study thus contributes to reducing the uncertainties associated with future changes in near-surface winds in cyclones (cf. Catto et al., 2019) through improved process understanding. In the second part of this study, Lagrangian airstream analyses will be used to complement and expand these dynamical insights.

Author contributions. SP and EDT designed the study. EDT performed the analysis, with support of FT for the PPVI, produced the figures, and drafted the manuscript. All authors discussed the results and edited the manuscript.

References

Ahmadi-Givi, F., Graig, G., and Plant, R.: The dynamics of a mid-latitude cyclone with very strong latent-heat release, Q. J. Roy. Meteorol. Soc., 130, 295–323, https://doi.org/10.1256/qj.02.226, 2004.

Barnes, S. L. and Colman, B. R.: Quasigeostrophic diagnosis of cyclogenesis associated with a cutoff extratropical cyclone-The Christmas 1987 storm, Mon. Weather Rev., 121, 1613–1634, https://doi.org/10.1175/1520-0493(1993)121<1613:QDOCAW>2.0.CO;2, 1993.

Bengtsson, L., Hodges, K. I., and Keenlyside, N.: Will extratropical storms intensify in a warmer climate?, J. Climate, 22, 2276–2301, https://doi.org/10.1175/2008JCLI2678.1, 2009.

Bjerknes, J.: On the structure of moving cyclones, Mon. Weather Rev., 47, 95–99, https://doi.org/10.1175/1520-0493(1919)47<95:OTSOMC>2.0.CO;2, 1919.

Bluestein, H. B.: Synoptic-dynamic Meteorology in Midlatitudes: Observations and theory of weather systems, Vol. 2, Taylor & Francis, ISBN: 0-19-506268-X, 198 Madison Avenue, New York, New York 10016-4314, 1992.

Brennan, M. J., Lackmann, G. M., and Mahoney, K. M.: Potential vorticity (PV) thinking in operations: The utility of nonconservation, Weather Forecast., 23, 168–182, https://doi.org/10.1175/2007WAF2006044.1, 2008.

Browning, K.: The sting at the end of the tail: Damaging winds associated with extratropical cyclones, Quarterly Journal of the Royal Meteorological Society: A journal of the atmospheric sciences, Appl. Meteor. Phys. Oceanogr., 130, 375–399, https://doi.org/10.1256/qj.02.143, 2004.

Browning, K. A.: Organization of clouds and precipitation in extratropical cyclones, in: Extratropical cyclones, 129–153, Springer, edited by: Newton, C. W. and Holopainen, E. O., First edition, https://doi.org/10.1007/978-1-944970-33-8_8, 1990.

Büeler, D. and Pfahl, S.: Potential vorticity diagnostics to quantify effects of latent heating in extratropical cyclones. Part I: Methodology, J. Atmos. Sci., 74, 3567–3590, https://doi.org/10.1175/JAS-D-17-0041.1, 2017.

Büeler, D. and Pfahl, S.: Potential Vorticity Diagnostics to Quantify Effects of Latent Heating in Extratropical Cyclones. Part II: Application to Idealized Climate Change Simulations, J. Atmos. Sci., 76, 1885–1902, https://doi.org/10.1175/JAS-D-18-0342.1, 2019.

Čampa, J. and Wernli, H.: A PV perspective on the vertical structure of mature midlatitude cyclones in the Northern Hemisphere, J. Atmos. Sci., 69, 725–740, https://doi.org/10.1175/JAS-D-11-050.1, 2012.

Catto, J.: Extratropical cyclone classification and its use in climate studies, Rev. Geophys., 54, 486–520, https://doi.org/10.1002/2016RG000519, 2016.

Catto, J., Jakob, C., Berry, G., and Nicholls, N.: Relating global precipitation to atmospheric fronts, Geophys. Res. Lett., 39, L10805, https://doi.org/10.1029/2012GL051736, 2012.

Catto, J. L. and Pfahl, S.: The importance of fronts for extreme precipitation, J. Geophys. Res.-Atmos., 118, 10–791, https://doi.org/10.1002/jgrd.50852, 2013.

Catto, J. L., Shaffrey, L. C., and Hodges, K. I.: Can climate models capture the structure of extratropical cyclones?, J. Climate, 23, 1621–1635, https://doi.org/10.1175/2009JCLI3318.1, 2010.

Catto, J. L., Ackerley, D., Booth, J. F., Champion, A. J., Colle, B. A., Pfahl, S., Pinto, J. G., Quinting, J. F., and Seiler, C.: The Future of Midlatitude Cyclones, Curr. Clim. Change Rep., 5, 407–420, https://doi.org/10.1007/s40641-019-00149-4, 2019.

Chang, E. K., Lee, S., and Swanson, K. L.: Storm track dynamics, J. Climate, 15, 2163–2183, https://doi.org/10.1175/1520-0442(2002)015<02163:STD>2.0.CO;2, 2002.

Charney, J.: The use of the primitive equations of motion in numerical prediction, Tellus, 7, 22–26, https://doi.org/10.1111/j.2153-3490.1955.tb01138.x, 1955.

Clark, P. A. and Gray, S. L.: Sting jets in extratropical cyclones: A review, Q. J. Roy. Meteorol. Soc., 144, 943–969, https://doi.org/10.1002/qj.3267, 2018.

Dacre, H., Hawcroft, M., Stringer, M., and Hodges, K.: An extratropical cyclone atlas: A tool for illustrating cyclone structure and evolution characteristics, B. Am. Meteorol. Soc., 93, 1497–1502, https://doi.org/10.1175/BAMS-D-11-00164.1, 2012.

Davis, C. A.: Piecewise potential vorticity inversion, J. Atmos. Sci., 49, 1397–1411, https://doi.org/10.1175/1520-0469(1992)049<1397:PPVI>2.0.CO;2, 1992.

Davis, C. A. and Emanuel, K. A.: Potential vorticity diagnostics of cyclogenesis, Mon. Weather Rev., 119, 1929–1953, https://doi.org/10.1175/1520-0493(1991)119<1929:PVDOC>2.0.CO;2, 1991.

Day, J. J., Holland, M. M., and Hodges, K. I.: Seasonal differences in the response of Arctic cyclones to climate change in CESM1, Clim. Dynam., 50, 3885–3903, https://doi.org/10.1007/s00382-017-3767-x, 2018.

Dee, D. P., Uppala, S., Simmons, A., Berrisford, P., Poli, P., Kobayashi, S., Andrae, U., Balmaseda, M., Balsamo, G., Bauer, D. P., Bechtold, P., Beljaars, A. C. M., van de Berg, L., Bidlot, J., Bormann, N., Delsol, C., Dragani, R., Fuentes, M., Geer, A. J., Haimberger, L., Healy, S. B., Hersbach, H., Hólm, E. V., Isaksen, L., Källberg, P., Köhler, M., Matricardi, M., McNally, A. P., Monge-Sanz, B. M., Morcrette, J.-J., Park, B.-K., Peubey, C., de Rosnay, P., Tavolato, C., Thépaut, J.-N., and Vitart, F.: The ERA-Interim reanalysis: Configuration and performance of the data assimilation system, Q. J. Roy. Meteorol. Soc., 137, 553–597, https://doi.org/10.1002/qj.828, 2011.

Deveson, A., Browning, K., and Hewson, T.: A classification of FASTEX cyclones using a height-attributable quasi-geostrophic vertical-motion diagnostic, Q. J. Roy. Meteorol. Soc., 128, 93–117, https://doi.org/10.1256/00359000260498806, 2002.

Donat, M. G., Leckebusch, G. C., Pinto, J. G., and Ulbrich, U.: European storminess and associated circulation weather types: future changes deduced from a multi-model ensemble of GCM simulations, Clim. Res., 42, 27–43, https://doi.org/10.3354/cr00853, 2010.

Ertel, H.: Ein neuer hydrodynamischer Wirbelsatz, Meteorol. Z., 59, 277–281, 1942.

Flaounas, E., Gray, S. L., and Teubler, F.: A process-based anatomy of Mediterranean cyclones: from baroclinic lows to tropical-like systems, Weather Clim. Dynam., 2, 255–279, https://doi.org/10.5194/wcd-2-255-2021, 2021.

Grams, C. M., Wernli, H., Böttcher, M., Čampa, J., Corsmeier, U., Jones, S. C., Keller, J. H., Lenz, C.-J., and Wiegand, L.: The key role of diabatic processes in modifying the upper-tropospheric wave guide: a North Atlantic case-study, Q. J. Roy. Meteorol. Soc., 137, 2174–2193, https://doi.org/10.1002/qj.891, 2011.

Grise, K. M. and Polvani, L. M.: The response of midlatitude jets to increased CO_2: Distinguishing the roles of sea surface temperature and direct radiative forcing, Geophys. Res. Lett., 41, 6863–6871, https://doi.org/10.1002/2014GL061638, 2014.

Hawcroft, M., Shaffrey, L., Hodges, K., and Dacre, H.: How much Northern Hemisphere precipitation is associated with extratropical cyclones?, Geophys. Res. Lett., 39, L24809, https://doi.org/10.1029/2012GL053866, 2012.

Hewson, T. D. and Neu, U.: Cyclones, windstorms and the IMILAST project, Tellus A, 67, 27128, https://doi.org/10.3402/tellusa.v67.27128, 2015.

Hodges, K.: Adaptive constraints for feature tracking, Mon. Weather Rev., 127, 1362–1373, 1999.

Hoskins, B. J., McIntyre, M. E., and Robertson, A. W.: On the use and significance of isentropic potential vorticity maps, Q. J. Roy. Meteorol. Soc., 111, 877–946, https://doi.org/10.1002/qj.49711147002, 1985.

Houze Jr., R. A.: Cloud dynamics, Academic press, 432 pp. ISBN: 9780080921464, 2014.

Kay, J. E., Deser, C., Phillips, A., Mai, A., Hannay, C., Strand, G., Arblaster, J. M., Bates, S., Danabasoglu, G., Edwards, J., Holland, M., Kushner, P., Lamarque, J.-F., Lawrence, D., Lindsay, K., Middleton, A., Munoz, E., Neale, R., Oleson, K., Polvani, L., and Vertenstein, M.: The Community Earth System Model (CESM) large ensemble project: A community resource for studying climate change in the presence of internal climate variability, B. Am. Meteorol. Soc., 96, 1333–1349, https://doi.org/10.1175/BAMS-D-13-00255.1, 2015.

Klawa, M. and Ulbrich, U.: A model for the estimation of storm losses and the identification of severe winter storms in Germany, Nat. Hazards Earth Syst. Sci., 3, 725–732, https://doi.org/10.5194/nhess-3-725-2003, 2003.

Lackmann, G. M.: Cold-frontal potential vorticity maxima, the low-level jet, and moisture transport in extratropical cyclones, Mon. Weather Rev., 130, 59–74, https://doi.org/10.1175/1520-0493(2002)130<0059:CFPVMT>2.0.CO;2, 2002.

Lamarque, J.-F., Bond, T. C., Eyring, V., Granier, C., Heil, A., Klimont, Z., Lee, D., Liousse, C., Mieville, A., Owen, B., Schultz, M. G., Shindell, D., Smith, S. J., Stehfest, E., Van Aardenne, J., Cooper, O. R., Kainuma, M., Mahowald, N., McConnell, J. R., Naik, V., Riahi, K., and van Vuuren, D. P.: Historical (1850–2000) gridded anthropogenic and biomass burning emissions of reactive gases and aerosols: methodology and application, Atmos. Chem. Phys., 10, 7017–7039, https://doi.org/10.5194/acp-10-7017-2010, 2010.

Lamarque, J.-F., Kyle, G. P., Meinshausen, M., Riahi, K., Smith, S. J., van Vuuren, D. P., Conley, A. J., and Vitt, F.: Global and regional evolution of short-lived radiatively-active gases and aerosols in the Representative Concentration Pathways, Clim. Change, 109, 191–212, https://doi.org/10.1007/s10584-011-0155-0, 2011.

Leckebusch, G. C. and Ulbrich, U.: On the relationship between cyclones and extreme windstorm events over Europe under climate change, Global Planet. Change, 44, 181–193, 2004.

Leckebusch, G. C., Koffi, B., Ulbrich, U., Pinto, J. G., Spangehl, T., and Zacharias, S.: Analysis of frequency and intensity of European winter storm events from a multi-model perspective, at synoptic and regional scales, Clim. Res., 31, 59–74, https://doi.org/10.3354/cr031059, 2006.

Madonna, E., Wernli, H., Joos, H., and Martius, O.: Warm conveyor belts in the ERA-Interim dataset (1979–2010), Part I: Climatology and potential vorticity evolution, J. Climate, 27, 3–26, https://doi.org/10.1175/JCLI-D-12-00720.1, 2014.

Marciano, C. G., Lackmann, G. M., and Robinson, W. A.: Changes in US East Coast cyclone dynamics with climate change, J. Climate, 28, 468–484, https://doi.org/10.1175/JCLI-D-14-00418.1, 2015.

Martin, J. E.: The structure and evolution of a continental winter cyclone. Part I: Frontal structure and the occlusion process, Mon. Weather Rev., 126, 303–328, https://doi.org/10.1175/1520-0493(1998)126<0303:TSAEOA>2.0.CO;2, 1998.

Martínez-Alvarado, O., Gray, S. L., Hart, N. C., Clark, P. A., Hodges, K., and Roberts, M. J.: Increased wind risk from sting-jet windstorms with climate change, Environ. Res. Lett., 13, 044002, https://doi.org/10.1088/1748-9326/aaae3a, 2018.

McTaggart-Cowan, R., Gyakum, J., and Yau, M.: Moist component potential vorticity, J. Atmos.

Sci., 60, 166–177, https://doi.org/10.1175/1520-0469(2003)060<0166:MCPV>2.0.CO;2, 2003.

Meinshausen, M., Smith, S. J., Calvin, K., Daniel, J. S., Kainuma, M., Lamarque, J.-F., Matsumoto, K., Montzka, S., Raper, S., Riahi, K., Thomson, A., Velders, G. J. M., and van Vuuren, D. P. P.: The RCP greenhouse gas concentrations and their extensions from 1765 to 2300, Clim. Change, 109, 213–241, https://doi.org/10.1007/s10584-011-0156-z, 2011.

Michaelis, A. C., Willison, J., Lackmann, G. M., and Robinson, W. A.: Changes in winter North Atlantic extratropical cyclones in high-resolution regional pseudo–global warming simulations, J. Climate, 30, 6905–6925, https://doi.org/10.1175/JCLI-D-16-0697.1, 2017.

Mölter, T., Schindler, D., Albrecht, A. T., and Kohnle, U.: Review on the projections of future storminess over the North Atlantic European region, Atmosphere, 7, 1–60, https://doi.org/10.3390/atmos7040060, 2016.

NCAR: National Center for Atmospheric Research, CESM [data set], https://www.cesm.ucar.edu/models/cesm1.0/, last access: March 2022.

Neu, U., Akperov, M. G., Bellenbaum, N., Benestad, R., Blender, R., Caballero, R., Cocozza, A., Dacre, H. F., Feng, Y., Fraedrich, K., Grieger J, Gulev S, Hanley, J., Hewson, T., Inatsu, M., Keay, K., Kew, S. F., Kindem, I., Leckebusch, G. C., Liberato, M. L. R., Lionello, P., Mokhov, I. I., Pinto, J. G., Raible, C. C., Reale, M., Rudeva, I., Schuster, M., Simmonds, I., Sinclair, M., Sprenger, M., Tilinina, N. D., Trigo, I. F., Ulbrich, S., Ulbrich, U., Wang, X. L., and Wernli, H.: IMILAST: A community effort to intercompare extratropical cyclone detection and tracking algorithms, B. Am. Meteorol. Soc., 94, 529–547, https://doi.org/10.1175/BAMS-D-11-00154.1, 2013.

O'Gorman, P. A.: Understanding the varied response of the extratropical storm tracks to climate change, P. Natl. Acad. Sci. USA, 107, 19176–19180, https://doi.org/10.1073/pnas.1011547107, 2010.

O'Gorman, P. A. and Schneider, T.: Energy of midlatitude transient eddies in idealized simulations of changed climates, J. Climate, 21, 5797–5806, https://doi.org/10.1175/2008JCLI2099.1, 2008.

Pfahl, S. and Sprenger, M.: On the relationship between extratropical cyclone precipitation and intensity, Geophys. Res. Lett., 43, 1752–1758, https://doi.org/10.1002/2016GL068018, 2016.

Pfahl, S., Madonna, E., Boettcher, M., Joos, H., and Wernli, H.: Warm conveyor belts in the ERA-Interim dataset (1979–2010). Part II: Moisture origin and relevance for precipitation, J. Climate, 27, 27–40, https://doi.org/10.1175/JCLI-D-13-00223.1, 2014.

Pfahl, S., O'gorman, P. A., and Singh, M. S.: Extratropical cyclones in idealized simulations of changed climates, J. Climate, 28, 9373–9392, https://doi.org/10.1175/JCLI-D-14-00816.1, 2015.

Pinto, J. G. and Ludwig, P.: Extratropical cyclones over the North Atlantic and western Europe during the Last Glacial Maximum and implications for proxy interpretation, Clim. Past, 16, 611–626, https://doi.org/10.5194/cp-16-611-2020, 2020.

Pinto, J. G., Zacharias, S., Fink, A. H., Leckebusch, G. C., and Ulbrich, U.: Factors contributing to the development of extreme North Atlantic cyclones and their relationship with the NAO, Clim. Dynam., 32, 711–737, https://doi.org/10.1007/s00382-008-0396-4, 2009.

Pinto, J. G., Gómara, I., Masato, G., Dacre, H. F., Woollings, T., and Caballero, R.: Large-scale dynamics associated with clustering of extratropical cyclones affecting Western Europe, J. Geophys. Res.-Atmos., 119, 13–704, https://doi.org/10.1002/2014JD022305, 2014.

Priestley, M. D. K. and Catto, J. L.: Future changes in the extratropical storm tracks and cyclone intensity, wind speed, and structure, Weather Clim. Dynam. Discuss. [preprint], https://doi.org/10.5194/wcd-2021-75, in review, 2021.

Raible, C. C., Messmer, M., Lehner, F., Stocker, T. F., and Blender, R.: Extratropical cyclone statistics during the last millennium and the 21st century, Clim. Past, 14, 1499–1514, https://doi.org/10.5194/cp-14-1499-2018, 2018.

Rivière, G., Gilet, J.-B., and Oruba, L.: Understanding the regeneration stage undergone by surface cyclones crossing a midlatitude jet in a two-layer model, J. Atmos. Sci., 70, 2832–2853, https://doi.org/10.1175/JAS-D-12-0345.1, 2013.

Roberts, J. F., Champion, A. J., Dawkins, L. C., Hodges, K. I., Shaffrey, L. C., Stephenson, D. B., Stringer, M. A., Thornton, H. E., and Youngman, B. D.: The XWS open access catalogue of extreme European windstorms from 1979 to 2012, Nat. Hazards Earth Syst. Sci., 14, 2487–2501, https://doi.org/10.5194/nhess-14-2487-2014, 2014.

Schneider, T., O'Gorman, P. A., and Levine, X. J.: Water vapor and the dynamics of climate changes, Rev. Geophys., 48, RG3001, https://doi.org/10.1029/2009RG000302, 2010.

Seiler, C.: A climatological assessment of intense extratropical cyclones from the potential vorticity perspective, J. Climate, 32, 2369–2380, https://doi.org/10.1175/JCLI-D-18-0461.1, 2019.

Shapiro, M. A. and Keyser, D.: Fronts, jet streams and the tropopause, in: Extratropical cyclones, 167–191, Springer, Boston, MA, https://doi.org/10.1007/978-1-944970-33-8_10, 1990.

Shaw, T., Baldwin, M., Barnes, E., Caballero, R., Garfinkel, C., Hwang, Y.-T., Li, C., O'Gorman, P., Rivière, G., Simpson, I., and Voigt, A.: Storm track processes and the opposing influences of climate change, Nat. Geosci., 9, 656–664, https://doi.org/10.1038/ngeo2783, 2016.

Sinclair, V. A., Rantanen, M., Haapanala, P., Räisänen, J., and Järvinen, H.: The characteristics and structure of extra-tropical cyclones in a warmer climate, Weather Clim. Dynam., 1, 1–25, https://doi.org/10.5194/wcd-1-1-2020, 2020.

Slater, T. P., Schultz, D. M., and Vaughan, G.: Acceleration of near-surface strong winds in a dry, idealised extratropical cyclone, Q. J. Roy. Meteorol. Soc., 141, 1004–1016, https://doi.org/10.1002/qj.2417, 2015.

Slater, T. P., Schultz, D. M., and Vaughan, G.: Near-surface strong winds in a marine extratropical cyclone: acceleration of the winds and the importance of surface fluxes, Q. J. Roy. Meteorol. Soc., 143, 321–332, https://doi.org/10.1002/qj.2924, 2017.

Sprenger, M., Fragkoulidis, G., Binder, H., Croci-Maspoli, M., Graf, P., Grams, C. M., Knippertz, P., Madonna, E., Schemm, S., Škerlak, B., and Wernli, H.: Global climatologies of Eulerian and Lagrangian flow features based on ERA-Interim, B. Am. Meteorol. Soc., 98, 1739–1748, https://doi.org/10.1175/BAMS-D-15-00299.1, 2017.

Stoelinga, M. T.: A potential vorticity-based study of the role of diabatic heating and friction in a numerically simulated baroclinic cyclone, Mon. Weather Rev., 124, 849–874, https://doi.org/10.1175/1520-0493(1996)124<0849:APVBSO>2.0.CO;2, 1996.

Tamarin, T. and Kaspi, Y.: The poleward motion of extratropical cyclones from a potential vorticity tendency analysis, J. Atmos. Sci., 73, 1687–1707, https://doi.org/10.1175/JAS-D-15-0168.1, 2016.

Tamarin, T. and Kaspi, Y.: The poleward shift of storm tracks under global warming: A Lagrangian perspective, Geophys. Res. Lett., 44, 10–666, https://doi.org/10.1002/2017GL073633, 2017.

Tamarin-Brodsky, T. and Kaspi, Y.: Enhanced poleward propagation of storms under climate change, Nat. Geosci., 10, 908–913, https://doi.org/10.1038/s41561-017-0001-8, 2017.

Teubler, F. and Riemer, M.: Dynamics of Rossby wave packets in a quantitative potential vorticity–potential temperature framework, J. Atmos. Sci., 73, 1063–1081, https://doi.org/10.1175/JAS-D-15-0162.1, 2016.

Tochimoto, E. and Niino, H.: Structural and environmental characteristics of extratropical cyclones that cause tornado outbreaks in the warm sector: A composite study, Mon. Weather Rev., 144, 945–969, https://doi.org/10.1175/MWR-D-15-0015.1, 2016.

Ulbrich, U., Leckebusch, G., and Pinto, J. G.: Extra-tropical cyclones in the present and future climate: a review, Theor. Appl. Climatol., 96, 117–131, https://doi.org/10.1007/s00704-008-0083-8, 2009.

Ulbrich, U., Leckebusch, G. C., Grieger, J., Schuster, M., Akperov, M., Bardin, M. Y., Feng, Y., Gulev, S., Inatsu, M., Keay, K., Kew, S. F., Liberato, M. L. R., Lionello, P., Mokhov, I. I., Neu, U., Pinto, J. G., Raible, C. C., Reale, M., Rudeva, I., Simmonds, I., Tilinina, N. D., Trigo, I. F., Ulbrich, S., Wang, X. L., and Wernli, H.: Are greenhouse gas signals of Northern Hemisphere winter extra-tropical cyclone activity dependent on the identification and tracking algorithm?, Meteorol. Z., 22, 61–68, https://doi.org/10.1127/0941-2948/2013/0420, 2013.

Wernli, B. H. and Davies, H. C.: A Lagrangian-based analysis of extratropical cyclones. I: The method and some applications, Q. J. Roy. Meteorol. Soc., 123, 467–489, https://doi.org/10.1002/qj.49712353811, 1997.

Wernli, H. and Schwierz, C.: Surface cyclones in the ERA-40 dataset (1958–2001). Part I: Novel identification method and global climatology, J. Atmos. Sci., 63, 2486–2507, https://doi.org/10.1175/JAS3766.1, 2006.

Wernli, H., Dirren, S., Liniger, M. A., and Zillig, M.: Dynamical aspects of the life cycle of the winter storm "Lothar" (24–26 December 1999), Q. J. Roy. Meteorol. Soc., 128, 405–429, https://doi.org/10.1256/003590002321042036, 2002.

Yettella, V. and Kay, J. E.: How will precipitation change in extratropical cyclones as the planet warms? Insights from a large initial condition climate model ensemble, Clim. Dynam., 49, 1765–1781, https://doi.org/10.1007/s00382-016-3410-2, 2017.

Zappa, G., Shaffrey, L. C., Hodges, K. I., Sansom, P. G., and Stephenson, D. B.: A multimodel assessment of future projections of North Atlantic and European extratropical cyclones in the CMIP5 climate models, J. Climate, 26, 5846–5862, https://doi.org/10.1175/JCLI-D-12-00573.1, 2013.

Zhang, Z. and Colle, B. A.: Impact of dynamically downscaling two CMIP5 models on the historical and future changes in winter extratropical cyclones along the East Coast of North America, J. Climate, 31, 8499–8525, https://doi.org/10.1175/JCLI-D-18-0178.1, 2018.